SLAC-PUB-656 (Rev.)
August 1969
(EXP)
Revised January 1972

ELASTIC ELECTRON-PROTON SCATTERING AT LARGE FOUR-MOMENTUM TRANSFER*

P. N. Kirk+, M. Breidenbach++, J. I. Friedman, G. C. Hartmann§ and H. W. Kendall,
Department of Physics and Laboratory for Nuclear Science,
Massachusetts Institute of Technology, Cambridge, Massachusetts 02139

G. Buschhorn**, D. H. Coward, H. DeStaebler, R. A. Early, J. Litt++,
A. Minten++, L. W. Mo§§, W. K. H. Panofsky and R. E. Taylor
Stanford Linear Accelerator Center, Stanford, California 94305

B. C. Barish, S. C. Loken+++, J. Mar*** and J. Pine
California Institute of Technology, Pasadena, California 91109

---

* Work Supported by the U. S. Atomic Energy Commission.

+ Present Address: Department of Physics, University of California-San Diego, San Diego, California 92037.

§ Present Address: Xerox Corporation, Rochester, New York.

** Present Address: DESY and the University of Hamburg, Hamburg, Germany.

++ Present Address: CERN, Geneva, Switzerland.

§§ Present Address: Department of Physics and the Enrico Fermi Institute, University of Chicago, Chicago, Illinois 60637.

*** Present Address: Bell Telephone Laboratories, Murray Hill, New Jersey.

+++ Present Address: Physics Department, Cornell University, Ithaca, New York.

(Submitted to Phys. Rev.)

ABSTRACT

Electron-proton elastic scattering cross sections have been measured at the Stanford Linear Accelerator Center for four-momentum transfers squared (q^2) from 1.0 to 25.0 $(GeV/c)^2$. The electric (G_{EP}) and magnetic (G_{MP}) form factors of the proton were not separated, since angular distributions were not measured at each q^2. However, values for G_{MP} were derived assuming various relations between G_{EP} and G_{MP}. Several theoretical models for the behavior of the proton magnetic form factor at high values of q^2 are compared with the data.

I. INTRODUCTION

Understanding the internal structures of elementary particles is a fundamental problem of strong interaction physics. More than fifteen years have elapsed since the early experiments of Hofstadter and collaborators at Stanford[1] showed the effects of the structure of the proton in elastic electron-proton scattering. During this time the problem of hadronic structure in general and nuclear structure in particular has received the the attention of experimentalists and theorists alike. The proton is the easiest hadron to study, and many available techniques can shed light on its structure. Of these techniques, high-energy elastic electron-proton scattering has proved to be particularly fruitful since the quantum electrodynamic's portion of the interaction is understood.

The momentum carried by the virtual photon responsible for the elastic scattering is reciprocally related to its wavelength and thus approximately reciprocally related to the characteristic distance probed in the interaction. One of the principal objectives of our experimental program was to make use of the high energy and high intensity electron beam at the Stanford Linear Accelerator Center (SLAC) to extend the kinematic range of the measurements of elastic electron-proton cross sections, and thus to search for structure effects at the shortest possible distances.

In the one-photon-exchange approximation, the structure of the proton is described by two functions, $G_{EP}(q^2)$ and $G_{MP}(q^2)$, the electric and magnetic structure form factors, respectively. These form factors depend only on the four-momentum transfer squared (q^2) to the proton, where

$$q^2 = 2E_oE(1 - \cos\theta) \qquad (1)$$

The quantities E_o and E are the incident and scattered electron energies, respectively, and θ is the laboratory scattering angle of the electron. Following the initial studies at Stanford, groups at Bonn, CEA, Cornell, DESY, Frascati, Orsay and Stanford measured elastic electron-proton cross sections to ever increasing values of q^2. Measurements[2] at DESY have extended the knowledge of $G_{MP}(q^2)$ to $q^2 = 10(GeV/c)^2$. Owing to greater experimental difficulty, $G_{EP}(q^2)$ has been measured[3] at DESY only to $q^2 = 3(GeV/c)^2$.

The program of elastic electron proton-scattering experiments at SLAC has measured $G_{MP}(q^2)$ to $q^2 = 25(GeV/c)^2$ and, with somewhat less precision, $G_{EP}(q^2)$ to $q^2 = 4(GeV/c)^2$. Our measurements of $G_{EP}(q^2)$ have been published earlier in letter form.[4] We here describe[5] the program of measurements of G_{MP} including detailed descriptions of the instrumentation, data reduction, and comparison of our results with other equivalent data and with a wide variety of the theoretical predictions.

The cross section for elastic electron-proton scattering has been calculated by Rosenbluth[6] in the approximation of a single-photon exchange process:

$$\left(\frac{d\sigma}{d\Omega}\right) = \left(\frac{d\sigma}{d\Omega}\right)_{NS} \left\{ \frac{G_{EP}^2 + \tau G_{MP}^2}{1 + \tau} + 2\tau\, G_{MP}^2 \tan^2 \frac{\theta}{2} \right\} \qquad (2)$$

where

$$\left(\frac{d\sigma}{d\Omega}\right)_{NS} = \left(\frac{e^2}{2E_o \sin^2 \frac{\theta}{2}}\right)^2 \frac{E}{E_o} \cos^2 \frac{\theta}{2} \qquad (3)$$

and

$$\tau = \frac{q^2}{4M^2} \qquad (4)$$

In Eq. (2), $\hbar=c=1$, the electron mass has been neglected, and M is the mass of the proton.

The interpretation of the form factors as Fourier transforms[7] of the spatial distributions of charge and magnetic moment of the proton is appropriate when q^2 is small enough so that the relativistic corrections are small. Although experiments in this region of q^2 have the advantage of straightforward interpretation, they have the disadvantage of being insensitive to details of the structure of the proton at small distances. The physical interpretation of the data at high values of q^2 is more difficult; however many of the theoretical models which have been advanced in recent years can be tested only in this region.

The Rosenbluth formula (Eq. (2)) relates one cross section to two form factors, and in order to determine experimentally both $G_{EP}(q^2)$ and $G_{MP}(q^2)$ as functions of q^2 the customary procedure is to measure the cross sections as functions of scattering angle at each value of q^2. This procedure leads to the "Rosenbluth plot" in which the structure-dependent part of the cross section is plotted as a function of $\tan^2\theta/2$ for a constant value of q^2. Thus Eq. (2) becomes

$$R = \frac{(d\sigma/d\Omega)}{(d\sigma/d\Omega)_{NS}} = I + S \tan^2\theta/2 \qquad (5)$$

with a slope:

$$S = 2\tau G_{MP}^2 \qquad (6)$$

and an intercept at $\tan^2\theta/2 = 0$:

$$I = \frac{G_{EP}^2 + \tau G_{MP}^2}{(1 + \tau)} \qquad (7)$$

By measuring the slope and the intercept, one can separate G_{EP} and G_{MP}. Unfortunately the separation becomes more difficult as q^2 increases because 1) the cross sections become smaller, and 2) the factor τ in the numerator of I enhances the contribution of G_{MP} relative to G_{EP}.

The following relationship is called "form factor scaling" (to distinguish it from "scaling" in deep inelastic electron scattering):

$$G_{EP}(q^2) = G_{MP}(q^2)/\mu \tag{8}$$

where μ is the magnetic moment of the proton. Form factor scaling is true by definition in the limit of $q^2 = 0$, and has been found experimentally[8] to be true to within about 5 percent for q^2 values up to $1(\text{GeV/c})^2$. More recent experiments[3,9] indicate that for values of q^2 up to $3(\text{GeV/c})^2$, form factor scaling is violated and that $G_{EP}(q^2)$ decreases faster with q^2 than $G_{MP}(q^2)$. These experiments support a two to three standard deviation violation of scaling. The SLAC data[4] are consistent with form factor scaling at q^2 of 2.5 and $3.75(\text{GeV/c})^2$ to within the measurement errors of about 40 percent; however they differ by only about 1.5 standard deviations from the results showing a violation of form factor scaling. By substituting Eq. (8) into Eq. (2), we have:

$$\left(\frac{d\sigma}{d\Omega}\right) = \left(\frac{d\sigma}{d\Omega}\right)_{NS} \left(\frac{G_{MP}^S(q^2)}{\mu}\right)^2 \left[\frac{1 + \mu^2\tau}{1 + \tau} + 2\tau\,\mu^2 \tan^2 \frac{\theta}{2}\right]. \tag{9}$$

which is the relation used in the present study to extract values of $G_{MP}^S(q^2)$. The superscript, S, denotes that G_{MP} is derived under the assumption of form factor scaling.

Hofstadter and his collaborators[10] found empirically that the form factors could be simply expressed by a relation which is now

referred to as the "dipole" formula:

$$G_{EP}^{D}(q^2) = \frac{G_{MP}^{D}(q^2)}{\mu} = G_{Dipole} = \frac{1}{(1 + q^2/0.71)^2} \qquad (10)$$

where q^2 has the units of $(GeV/c)^2$. This relationship incorporates the form factor scaling rule. Although the existing data show statistically significant deviations form Eq. (10), it remains a useful approximation of the form factors over a wide range of q^2.

Most of the data of the present experiment were taken for q^2 values larger than $4(GeV/c)^2$ but, as angular distributions were not taken at each q^2 value, it was not possible to check the validity of Eq. (8). In this paper the correctness of form factor scaling will not be analyzed further.

II. THE EXPERIMENTAL EQUIPMENT

II.1 Brief Description

The data which we report were taken over a period of about two years at the Stanford Linear Accelerator Center (SLAC) by a collaboration of physicists from the Massachusetts Institute of Technology, California Institute of Technology, and SLAC. Views of the experimental arrangement are given in Fig. 1. The electron beam from the linear accelerator passed through a liquid hydrogen target and the scattered particles were analyzed with the SLAC 8-GeV/c magnetic spectrometer. The total charge incident upon the target in each run was measured by secondary-emission monitors (SEM) and a toroid induction monitor. These monitors were regularly intercalibrated using a Faraday cup. Particles which had

passed through the spectrometer were detected by a system of scintillation counter hodoscopes, dE/dx counters and a total absorption shower counter. The scintillation counters through which a particle passed were identified in the electronics by a coincidence technique which set flip-flops in a buffer array. An on-line computer scanned the buffers, read the pulse-heights in the dE/dx and shower counters, and recorded the information on magnetic tape for later off-line analysis. The computer also performed extensive equipment tests and on-line calculations.

As these were the first measurements performed with the 8-GeV/c spectrometer, we included detailed check runs to investigate the optics of the device and, in particular, to measure the variation of the solid angle acceptance for different momentum settings. (For further details, see Section IV.1). We also measured cross sections as a function of beam spot size, beam current intensity, and pulse repetition rate in order to investigate density changes in the liquid hydrogen (see Section IV.2).

In the balance of this section we give a more detailed description of the experiment and the apparatus. In Section III we discuss the details of the data analysis.

II.2 The Beam

The beam transport system consisted of bending magnets and quadrupoles which provided a momentum-analyzed and focussed beam at the target. The maximum phase space through the system in both horizontal and vertical directions was roughly equivalent to 0.3 cm beam spot radius times 10^{-4} radian angular divergence. A simplified drawing of the optics of the transport system is given in Fig. 2. The beam from

the accelerator[11] was collimated and passed through the first bending magnet (BM1) and then through momentum-defining slits (S). Quadrupoles imaged the collimator onto the slits. The slits could be adjusted to define a total momentum pass band ($\Delta p/p$) in the range from 0.1 to 2.5%. The beam was then transmitted through the second bending magnet (BM2) and with quadrupoles refocused onto the target. The focussing was achromatic, that is, after leaving the last magnetic element, the momentum and transverse position distribution within the beam were uncorrelated.

The accelerator delivered up to 360 pulses of beam per second, with a pulse length which varied between 1.0 and 1.5μsec. During these measurements, time-averaged currents of up to 10μA were used, although the intensity had to be reduced by about a factor of from 10 to 50 for the low-q^2 data.

The total momentum spread in the incident beam was restricted between typically 0.1 and 0.2% so that a kinematic separation could be maintained between the elastic electron-proton scattering peak and inelastic threshold. Precise knowledge of the incident energy was required since the cross section varied rapidly with energy. Extensive magnetic measurement and precision surveying of the beam transport system provided a momentum and hence energy calibration to an accuracy of between ±0.1 and ±0.2%. The incident momentum was determined from the reading of a flip-coil magnetometer in a reference magnet identical to and connected in series with the bending magnets. It is believed that the system would reproduce a given momentum to within ±0.02%.

The analyzed beam entered the experimental area through a channel in a heavy shielding wall. By adjustment of upstream steering magnets and by monitoring the position of the beam on two zinc-sulfide-coated

screens (S1 and S2 in Fig. 1), the position of the beam at the target was aligned to within about 1 mm and the incident beam direction determined to better than 0.1mrad. The beam spot size at the target was approximately elliptical in shape with vertical and horizontal widths about about 3 and 6 mm, respectively.

To minimize backgrounds arising from disposal of the main beam, the beam traversed the experimental area to a beam dump located about 70 m behind the target area.

II.3 Beam Current Monitors

The main current monitor for this experiment was a toriod induction device[12]. It consisted of a ferrite toroidal-shaped core which was located in the incident beamline such that the beam passed through its 4-inch diameter aperture. A winding on the toroid was loaded with a capacitor, resulting in a circuit resonant at 5.5 kHz. Electron beam pulses excited resonant oscillations in this circuit. The resonant signal appearing across the toroid terminals was amplified and the waveform sampled at one of its subsequent maxima. This sampled voltage was proportional to the beam charge. The circuitry was designed to have extremely low noise, high stability, and adequate reliability.

The toroid monitor was remotely reset, started, stopped and read by the on-line computer. The toroid core contained an additional winding through which a known amount of charge could be transmitted, simulating a beam pulse, for the purpose of absolute calibration.

At regular intervals in the data-taking, the SLAC Faraday cup[13] was brought into the beamline to intercalibrate the current monitors.

The absolute efficiency of the Faraday cup was taken to be 100.0 ±0.2%.[13] The toroid monitor was calibrated with respect to the Faraday cup to within a few tenths of one percent. The long-term stability of the toroid for the beam levels of this experiment was found to be better than ±0.5%.

As an additional check on beam monitoring, we used two secondary-emission monitors positioned after the liquid hydrogen target. In order to obtain the best stability, several designs[14] for this type of monitor were used. At best, the responses of these devices would vary by a few percent depending upon the history of their irradiation and also depending upon the energy of the incident beam. Although they were useful for short-term checks of the toroid monitors, these devices were not found to be suitable as main monitors in the experiment.

II.4 Liquid Hydrogen Target

Five condensation-type[15] liquid hydrogen target cells of different size (vertical cylinders 8 to 32 cm diameter with 25 to 75 μ thick stainless steel walls) were used during this experiment. Pure hydrogen gas at a pressure of 15 psig was cooled and liquified by contact with a large reservoir of liquid hydrogen at 20.4°K and atmospheric pressure. The liquid hydrogen then passed into the thin-walled target cell which was cooled by a copper heat exchanger coupled to the hydrogen reservoir. The pressure of the hydrogen gas kept the temperature of the liquid hydrogen in the target cell about 2.5°K below its boiling point.

In Fig. 3 we show the hydrogen target cell, the "dummy" (empty) cell which was positioned below the hydrogen target cell, and also a location

for a solid target. Any one of these three could be moved remotely into the electron beam.

Relative target temperature changes were measured by carbon resistors and hydrogen vapor pressure thermometers[16] immersed in the liquid hydrogen of the target cell. The absolute calibration of the thermometers was made by reducing the pressure on the target cell until the liquid just began to boil. From pressure-temperature tables for liquid hydrogen[17] we established that the mean cell temperature was 21.0°K, corresponding to a liquid hydrogen density of 0.07035 gcm^{-3}. We estimated that the absolute accuracy of the density determination was ±1.5%.

II.5 The 8-GeV/c Magnetic Spectrometer

The Spectrometer Facility at SLAC consists of three magnetic spectrometers, capable of analyzing particles up to momenta of 1.6 GeV/c, 8 GeV/c and 20 GeV/c, respectively.[18,19,20] All rotate on concentric rails about a common vertical axis and target position. The variation of kinematics and expected cross sections suggested that it was most feasible to cover the range of scattering angles from 0° to 180° with three instruments. The 20-GeV/c spectrometer is used for small angle measurements (0° to 20°, with about 100 microsteradians of solid angle), the 8-GeV/c spectrometer for intermediate angles (12° to 100°, with about 750 microsteradians of solid angle) and the 1.6-GeV/c spectrometer for backward angles (25° to 165°, with about 3 millisteradians of solid angle).

The kinematics of most high-energy physics reactions in which a single particle is detected in the final state imply that if good momentum resolution of the detected particle is required, then it is also necessary to determine the scattering angle at which the particle is produced or

scattered to an accuracy better than that defined by the angular acceptance of the spectrometer. On the other hand, normally one is not interested in knowing the precise position in the target where the reaction took place. Therefore, all three spectrometers were designed to focus point-to-point from target to image plane in the vertical (bend) plane and line-to-point in the horizontal plane. The momentum of a transmitted particle is dispersed in the vertical plane while the production angle relative to the central orbit of the spectrometer is dispersed in the horizontal plane.

The 8-Gev/c spectrometer was chosen for this experiment because it combined a large solid angle acceptance with the momentum and angular ranges necessary to adequately detect those electrons which elastically scattered at large q^2.

The spectrometer is composed of three quadrupoles (Q81, Q82 and Q83) which provide the required focussing, and two rectangular, n=0, 15° bending magnets (B81 and B82) which provide the momentum dispersion. The arrangement of the magnets and the first-order focal properties are shown in Figs. 4a and 4b. The spectrometer has a maximum solid angle acceptance of greater than 0.75 millisteradian, an acceptance of 20 centimeters in target length projected perpendicular to the central ray, and a momentum acceptance of ±2%. The measured first-order dispersions at 8 GeV/c are 4.57 cm per milliradian in production angle, and 2.91 cm per percent in momentum. The total horizontal and vertical angular acceptances are 15.6 and 59.0 milliradians respectively. Because of the large chromatic aberrations, the momentum focal plane is tipped at an angle of 13.7° to the central ray. The production-angle focal plane is kept perpendicular to the central ray because it is not affected

strongly by the second-order aberrations. It is separated from the center of the momentum focal plane by 0.5 meter to allow separate angle and momentum measurements by two hodoscopes, one lying in each focal plane. In these two focal planes, the resolutions calculated from the design values of the first- and second-order coefficients are ±0.05% in momentum (assuming a vertical beam size at the target of ±0.15 cm) and ±0.2 milliradian in horizontal production angle. The main spectrometer parameters are tabulated in Table I. Further discussion of the optical properties of the spectrometer as well as the results of detailed tests of the optics and measurements of the acceptance apertures will be given in Section IV.1.

The energy resolution requirement was determined by the kinematics for separating elastic electron-proton scattering from the threshold for the production of a single pion. This separation, S, is approximately given by:

$$\frac{S}{P} = \frac{m_\pi}{E_o} \tag{11}$$

where m_π is the pion mass. The most critical requirement for momentum resolution was for E_o = 20 GeV (at the maximum SLAC machine energy) when S/p = 0.7%. To be certain of achieving a clean separation, the detectors were built with a momentum resolution of 0.1% in $\Delta p/p$. From elastic electron-proton scattering kinematics the required resolution ($\Delta\theta$) to match a given momentum resolution is given by:

$$\Delta\theta = \left(\frac{\Delta p}{p}\right)\left(\frac{M}{p \sin\theta}\right) \tag{12}$$

As seen in Fig. 5a, the smallest value of $\Delta\theta$ for elastic e-p scattering

with E_o = 20 GeV (assuming $\Delta p/p = 0.1\%$) is about 0.3 milliradian. Thus, to be consistent with the design resolution of the momentum hodoscope, the θ-hodoscope was built with a first-order optics resolution of 0.3 milliradian.

The complete spectrometer assembly, including the magnets, carriage, detector boom and shielding is shown in Fig. 6. The magnets were mounted on the carriage in such a way that they could be aligned relative to one another with sufficient accuracy to insure the resolutions mentioned above. The detectors were mounted on a boom extending out beyond Q83. The iron and concrete detector shielding was carried on a set of two separate shielding carriages which opened and closed around the detectors like a clam shell.

The locations of each magnet element and detector positions were determined by optical surveying and were monitored during the experiment by a position sensing system[21]. This system consisted of differential magnetic transformers clamped to the magnetic components with two parallel stretched wires passing through them firmly held from the detector and target ends of the support structure. The wires carried a 10 kHz current which would induce voltages in the transformers when the transformers were displaced. The induced voltages were read into the on-line computer from four transformers located on each magnet. From the information, the computer calculated the three coordinates of the center of each magnet (x, y and z) and the three rotations (pitch, roll and yaw) and compared the values with allowed values. The position stability was checked over several weeks and found to be satisfactory, representing position changes which would affect the momentum resolution by less than 0.02% in $\Delta p/p$.

The properties of the magnets are given in Table II. Magnet currents were set by the on-line computer, allowing the remote setting of the momentum for the complete spectrometer or for an individual magnet. The current in each set of magnet coils was read by the computer using a standard calibrated shunt and a precision digital voltmeter and the readings were compared with the calculated settings. The stability of the magnet power supplies and accuracy of the computer control and readout system allowed a reproducibility in the setting of the spectrometer momentum to an accuracy of better than ±0.02% in $\Delta p/p$. The absolute calibration of p, from magnetic measurements and using elastic e-p scattering kinematics, agreed with the calibration of the beam switchyard momentum within about ±0.15%.

The horizontal scattering angle setting of the spectrometer was set manually by a chain, sprocket, and shaft encoder system to a precision of about 0.001 degree. The absolute accuracy of the angle system with respect to a defined incident beamline was better than ±0.15 milliradian.

The actual momentum resolution of the complete optical system was degraded by several factors:

1) The beam spot size at the target. A change in the vertical beam height at the target of 3.0 mm will cause an apparent shift in p by about 0.1% at the focal plane. We employed a total vertical spot size of about 3 mm and vertical excursions of the beam position were monitored to within about ±0.5 mm.

2) The quality of the incident beam. The angular divergence of the primary beam was less than ±0.1 milliradian and thus had only a small effect on the spectrometer resolution. The direction of the incident beam was maintained to within ±0.1 milliradian during data taking.

The effect of the momentum resolution of the incident beam ($\Delta E_o/E_o$) on the percentage spread $\Delta p/p$ for elastic e-p scattering is given by:

$$\frac{\Delta p}{p} = \frac{1}{\left(1 + \frac{2E_o}{M} \cdot \sin^2 \frac{\theta}{2}\right)} \cdot \frac{\Delta E_o}{E_o} = \frac{p}{E_o} \cdot \frac{\Delta E_o}{E_o} \qquad (13)$$

This variation is shown in Fig. 5b which indicates that the highest resolution of the beam switchyard system ($\Delta E_o/E_o = 0.1\%$) was rarely required, and for larger scattering angles the momentum-defining slits could be widened to increase the beam current while preserving an acceptable resolution.

3) Multiple scattering. According to Eq. (12) multiple scattering in the target material broadened the apparent $\Delta p/p$ of the scattered beam. The effect on $\Delta p/p$ of multiple scattering of the lower momentum scattered electron was larger than that of the incident electron. For example, for elastic e-p cross section measurements taken with an 0.02 radiation length cylindrical target at $q^2 = 15(\text{GeV/c})^2$, and a scattering angle of 19.7^o, the multiple scattering of the incident (16 GeV) and scattered (8 GeV) electrons contributed to the percentage spread $\Delta p/p$ by 0.027% and 0.054%, respectively.

4) Second-order aberrations in the optics. As seen later (Section IV.1) these effects are small.

5) Energy-loss processes. The effect of electron energy-loss by radiation was to broaden the momentum spectrum of the scattered electrons. (Radiative corrections will be discussed in detail in Section III.3) The increase in energy spread from Landau straggling in the target material was negligibly small in these experiments.

6) Target length. For a target of finite length there was a "depth of field" effect arising from second-order aberrations associated with the change in apparent target length for varying scattering angle. For a 20 cm long target, this effect caused $\Delta p/p$ to increase by a factor of about 1.5 as the spectrometer moved from 90° to 15°.

7) Vertical acceptance. The finite vertical angular acceptance of ± 29.5 milliradians from the target made a negligible contribution to the momentum resolution at the angles of these measurements (greater than 12°).

II.6 The Detection System

The locations of the scattered particles at the θ- and p-focal planes were determined with two arrays of scintillation counters. Electrons were identified, and pions and background radiation rejected by a complex array of particle discrimination counters. Information from the detectors was partially processed electronically and then recorded in buffer storage before being read into the on-line computer. This section will describe the detectors, Section II.7 will give details of the electronics, and the computer system will be outlined in Section II.8.

From the design values of the θ- and p-dispersions and from the desired resolutions in θ and p it was found that the required horizontal resolution was 1.3 cm and the required vertical resolution was 0.3 cm. The final design for the hodoscopes is shown in Fig. 7. The θ-array was constructed in two banks, the front bank (nearest to the target) contained 27 scintillation counters and the rear 28 counters. The rear bank

was displaced laterally by a half of a counter width with respect to the front bank. Thus, each θ-bin was defined by the overlap region of a counter in the front and a counter in the rear bank. The p-array was similarly arranged in two banks, relatively displaced vertically by half of a counter width and containing 20 and 21 scintillation counters, respectively. Each momentum counter was 0.63 cm tall, 1.9 cm thick and 84 cm long, and each theta counter was 2.51 cm wide, 0.63 cm thick and 17.5 cm tall.

The two hodoscopes were bracketed by front and rear trigger counters, each of which contained five overlapping scintillators. A coincidence between these trigger counter scintillator arrays set a flag bit which was read into the computer and provided the information used in evaluating counter efficiencies. Since the trigger counters were slightly larger than the hodoscopes, particles could miss the two hodoscope arrays and still make a coincidence between the front and rear trigger counters.

The apparatus for particle identification was designed to separate electrons from background pions in both elastic and inelastic scattering measurements. For elastic electron-proton scattering, the discrimination between electrons and pions was most critical at high values of four-momentum transfer where the electron count rate became extremely low. The apparatus for π-e identification was a fairly elaborate system, although only two main items were required for this experiment. These parts, shown schematically in Fig. 7, were:

1) A total absorption shower counter. This device absorbed totally the energy of an incident electron, whereas most of the energy of an incident pion escaped. It had an electron detection efficiency

assumed to be 100%, and it misidentified pions as electrons in only a few percent of the pion events.

2) Three dE/dx counters. These counters were placed after a 1 radiation length lead radiator and served to determine the pulse-height differences between a minimum-ionizing pion and a showering electron. When used in conjunction with the total absorption counter, pions were rejected with a probability of only about 1 in 10^4 of misidentifying a pion as an electron. At this level of pion rejection, the efficiency of identifying electrons was reduced to about 80%.

The total absorption counter consisted of 16 alternating layers of lead (1 radiation length thick) and ultraviolet transmitting lucite (1.9 cm thick). It was followed by 15 radiation lengths of lead. Each slab of lucite was viewed by four two-inch diameter photomultiplier tubes. The energy deposited by a showering electron was sampled by measuring Cerenkov light in the lucite. The amount of lead in this counter absorbed most of an electromagnetic shower, but was not sufficient for the development and dissipation of a pion cascade shower.[22] The width of the pulse-height spectrum of electron showers was approximately inversely proportional to the square root of the electron momentum. Thus, for high-energy particles it was possible to obtain a clean separation between the electron and pion signals, except for the few percent of the pions which had sufficient pulse height to underlie the electron peak.

The three dE/dx counters were made from 1.3 cm thick plastic scintillator and were preceded by a 1 radiation length of lead slab. A high-energy electron passing through the lead produced from 4 to

8 minimum-ionizing particles. A pion had a probability of about 0.9 of not interacting in an absorber of this size. However, due to Landau straggling, there was a probability of a few percent that a pion signal could resemble the energy loss corresponding to two or three minimum ionizing particles. In the present arrangement, three dE/dx counters were used so that the probability of this occurring in all three counters was reduced to less than 0.5%. Although the dE/dx counters were not used in the final analysis of the elastic electron scattering data reported here, they were used very effectively in the diagnostic phase of the experiment.

A two inch thick lead mask was installed around the outside edges of the two hodoscope arrays and just behind the rear trigger counters. (see Fig. 7). This mask greatly reduced the probability that a particle that did not traverse the hodoscope assembly could deposit enough energy in the total absorption shower counter to fire the total absorption counter threshold discriminator.

II.7 The Electronic Arrangement

The electronic instrumentation was used to select events from the detectors and to record the information in buffer storage. Under computer command, this data was transferred to computer storage in the 2.8 msec time interval between accelerator pulses. A schematic of the electronics is given in Fig. 8.

An output pulse from the total absorption counter was fed into a threshold discriminator to provide a signal ("TA") for the triggering logic. The discriminated outputs from the 10 trigger counters were fed

into separate OR circuits for the front and rear trigger systems. A coincidence between any front and any rear trigger counter generated a signal ("TRIG") for the logic circuitry. The TRIG and TA pulses were both fed into an AND and an OR circuit. Outputs from these units generated interrupts for events to be stored in the computer and comprised the principal triggering logic. Since every particle which triggered the AND circuit also triggered the OR circuit, the AND circuit appears to be logically redundant. However, it was useful for the evaluation of deadtime effects, as explained later.

Signals from the 55 θ-counters and 41 p-counters were fed into DCD electronic modules (which consisted of an input discriminator, a coincidence circuit and output discriminator), each of which was followed by an element of buffer storage. The resolving time of the DCD circuit was approximately 30 nsec. Also fed through DCD's to buffers were the 10 trigger counter discriminators and the pulses TA, TRIG, AND, and OR. A total of 110 DCD modules were used in this experiment.

The principal trigger signal, developed as outlined above, was fanned out to supply the second input to the coincidence circuit of each DCD. In this manner all θ- and p-counters, and the other counters of the detection array, were interrogated following the arrival of a "candidate event" selected by the trigger logic.

The outputs of the total absorption counter and of the dE/dx counters were pulse-height analyzed and the digitized outputs also held in buffer storage.

The computer could read in the information from the buffers for only one event per beam pulse. A "kill" circuit was used in the logic to prevent counter pulses from more than one event from entering the

the buffer storage locations during one beam pulse. Scalers attached to the input and output of the kill circuit were used to determine the number of potential triggers rejected by this circuit and thus to provide a computer deadtime correction. The incident beam intensity was adjusted to keep the losses due to the kill circuit below about 15%.

A beam gate developed from an accelerator pretrigger pulse ensured that virtually all accepted events occurred within a time window of 5 μsec associated with the beam.

For this triggering logic, there were three classes of events:

Class:	1	2	3
TRIG pulse:	Yes	Yes	No
TA pulse:	Yes	No	Yes

Class 1: Approximately 95% of the elastic electron-proton scattering data were contained in this class. The threshold level of the TA discriminator was set low for most of the data taking to ensure producing an output pulse for all elastically scattered electrons. At this selected threshold level, many pions would also trigger the discriminator and so were included in Class 1. Class 2: These events were either from low pulse-height events in the TA counter of electronic inefficiencies. The deadtime contribution of the TA counter was negligible at the counting rates of this experiment. Class 3: Some of these events were scattered electrons which arrived during the deadtime (1 to 3%) of the trigger counters.

II.8 The On-line Computer

An SDS-9300 computer was employed on-line for data logging and reduction and for control of the experiment. It had a 24-bit word size, 32k words of core storage, a 1.75 μsec cycle time, and was large enough to provide flexible and extensive control of the experiment and analysis of the stored events. The details of the system, which was especially developed for the SLAC Spectrometer Facility, have been reported elsewhere.[23]

The primary function of the computer was to record on magnetic tape all the information for later off-line analysis of the data. For each scattered particle which passed through the detector system, the computer required 12 words to store such information as the contents of the buffer storage locations and the digitized outputs of the pulse-height analyzers. At the beginning and end of each run the computer read and logged additional miscellaneous data such as scaler values, beam-current monitor outputs, and the target and spectrometer magnet conditions. When otherwise unoccupied during runs the computer monitored the experimental equipment and data, performed simplified cross section calculations on-line, and updated graphical displays.

II.9 Choice of Running Conditions

For a given q^2, the cross section for elastic electron-proton scattering increases with decreasing electron scattering angle. The closest angle of approach of the 8-GeV/c spectrometer to the primary beam direction was about 12°. Thus, for low-q^2 values, the data were collected at angles near 12°. At higher q^2 values, the limiting

kinematic factor was either the maximum momentum setting of the spectrometer or the maximum available accelerator energy.

The momentum setting of the spectrometer was adjusted so that the peak from elastic e-p events appeared in the center of the p-θ hodoscope area. The peak lay along a line which was tilted with respect to the axes of the p-and θ-counters from the effect of the elastic scattering kinematics. The threshold setting for the TA counter discriminator was adjusted so that it fired for all the elastically scattered electrons and for an approximately equal number of pions. The incident beam intensity was adjusted so that the kill-circuit losses (mentioned in Section II.7) were about 15% or less, and the counting rate in the front trigger counter array was about 2 counts or less per 1.5 μsec beam pulse.

The measured cross sections varied between 3×10^{-32} and 2×10^{-39} cm^2/sr and the statistical accuracy from about 0.3% to about 35%. At most kinematic conditions, runs were made using the dummy (empty) target cell in order to correct for non-hydrogen-scattered events in the full target data. The subtraction from the full-target data for these events was typically 2 to 4%.

III. DATA ANALYSIS

The data analysis was divided into two main parts:

1) The selection of scattered electron events from the detector signals and the reconstruction of the locations in the θ-p arrays.

2) The calculation of cross section values from the selected raw data and the evaluation of the measurement errors. These topics will

be discussed in this section.

III.1 Event Selection

For each scattered event which was recorded on magnetic tape we had the following information:

1) Electronic logic condition: Whether the event fired (a) the fast trigger counters (TRIG) and/or (b) the total absorption shower counter (TA).

2) Hodoscope patterns: Knowledge of the counters which fired in the θ-p hodoscope arrays.

3) The π-e discriminator: Pulse-height information from the total absorption counter and the three dE/dx counters.

In off-line analysis one could reject about one-half of the data logged on magnetic tape (and reject only a few percent of the electron events) by requiring that each event be accompanied by a TRIG output and have a TA pulse height which exceeded a preselected minimum value. These are the event classes 1 and 2, mentioned earlier in Section II.7.

The clearest indication that a single-particle track passed through a hodoscope was that two counters fired, one in each of the two banks. Although the location of such a track is unambiguously defined, the presence of single additional counters which fired due to a background event or delta ray tended to confuse the pattern. Thus, in the analysis program we studied the bit patterns from the buffer storage for the θ- and p-hodoscopes and put each event into one of the following categories:

1) Good event: Each hodoscope had one single-particle track.

2) Ambiguous event: At least one hodoscope had two or more single-particle tracks. These were usually caused by elastically scattered electrons which produced a delta ray in or near the hodoscopes.

3) Bad event: At least one hodoscope had no evidence for the passage of a single particle through it.

The effects of imposing certain requirements on the data are illustrated in Fig. 9, which shows the TA spectrum on a logarithmic scale for a run at $q^2 = 2.5(\text{GeV/c})^2$ and $\theta = 12.6^\circ$, where $E_o = 7.9$ GeV and $E = 6.6$ GeV. Graph 9a shows the pulse-height distribution of all the raw data which were logged onto the magnetic tape. Logged data required the presence of a TA pulse that fired the associated TA-discriminator, a TRIG pulse, or both. The electron peak is clear, but there is noticeable contamination on the low-energy side of the peak. Graph 9b shows the spectrum when only a TA pulse is required (i.e. when the raw data were reanalyzed to select only those events which had a TA pulse that fired the associated TA-discriminator). Very low pulse heights are much reduced but the shoulder at channels 30-50 is little changed. Graph 9c shows the spectrum when only a TRIG signal is required. The very low pulse heights are little changed, but the shoulder is markedly reduced. Graph 9d shows the spectrum when only a good event is required in both of the hodoscopes. The background events are much reduced. Graph 9e shows the spectrum when all three requirements are included. Some of the events above channel 80 were double events, and others were single events which arrived in coincidence with an accidental in the TA counter. They were not background events in either case. The

electron peak was close to Gaussian in shape and there was evidence of a small amount of contamination only on the low-energy side of the peak.

There was a large range over which one could vary the minimum acceptable TA pulse height and eliminate only the very low pulse-height events. These latter events were studied in detail and, since we could find no evidence for the presence of elastically scattered electrons among them, they were discarded. For this typical spectrum, out of about 26,000 events in Fig. 9a, only about 12,000 were selected as good electrons for Fig. 9e, and of these about 80 were eliminated by the requirement for a specified minimum pulse height from the TA counter.

III.2 Track Location

There were many possibilities for patterns which could appear in the hodoscope arrays. In Table III we show the different types of patterns which the computer was programmed to recognize. For convenience, we show a 20-element hodoscope. The patterns are arranged in the three categories (good, ambiguous and bad events) which were outlined in Section III.1.

The hodoscope signals were routed to the buffer storage so that overlapping counters which fired appeared as adjacent set bits in the buffer. The exact assignment of a bin location depended upon the number of set bits. If an odd number of adjacent bits was set, the program selected the center bit to define the bin number. For an even number of adjacent set bits, the bin number was randomly chosen as the bit to the left or right of the middle of the set bits. In Table III, where a bin location was assigned, we have indicated its position with

an arrow, or a double arrow where randomizing was used.

Several types of patterns were used to be certain that events were not accidently lost or gained. The number of adjacent set bits was allowed to extend beyond the number expected from the hodoscope design (patterns 4, 5, and 11). Extra single bits were expected. If they accompanied a track with multi-adjacent bits, the single was assumed to be due to background (patterns 6, 8 and 9). However, if only single bits were present (patterns 1, 7 and 10), they could have been due to an inefficient hodoscope counter and were saved for further investigation. Some patterns which contained extra single set bits were so rare that there were too few events to evaluate them with certainty. As they could only have a negligible effect on the final cross section values they were included in patterns such as 6, 8 and 9.

All configurations, however exotic, fell into one of the patterns of Table III. An intensive study of the TA pulse-height spectra for events of different patterns and whether or not accompanied by a TRIG signal, together with mapping of the location of the patterns in the θ-p plane, indicated that this scheme was more elaborate than was ultimately required. However in aiming for an overall accuracy in decoding the events to better than $\pm 1\%$ it was necessary to check the details to substantially better accuracy. In retrospect, there was no need to distinguish between events with patterns 2 to 6, as they represented a clean sample of unambiguous, locatable tracks. When they were checked for having a TRIG output and an acceptable TA pulse height, they contributed approximately 95% of the final selected data.

To select from events which may have had a bit unset due to a single inefficient counter or to thin gaps between adjacent hodoscope counters (patterns 1 and 7) it was necessary to study the TA counter spectrum. The TA spectrum showed a clean electron peak only for the events which had a TRIG output and a good track in one hodoscope. These events were either populated uniformly throughout the θ-p plane (as expected if caused by gaps) or were located in regions containing known inefficient counters. Thus, by demanding the TRIG output, it was possible to add selected events from patterns 1 and 7 into the set of final selected data.

Pattern 8 provided most of the ambiguous events, and most of these events had no contamination due to extra single set bits. The double tracks were rarely due to two electrons in the system, which would have given a large TA pulse height, but were mainly caused by an electron accompanied by a delta ray.

The bad event class included tracks which had only the edge bit(s) set (pattern 13). This corresponded to a particle which traversed the outer half-width of the outside counters of the hodoscope. As we decided to restrict our data to those events falling within the region of overlapping counters, these events were rejected. Some of the blank hodoscope events (pattern 12) might have been due to a scattered particle which passed through two adjacent inefficient counters in a hodoscope. This type of event was rare except for one short period of running, when there was a deterioration in some of the p-counters which caused a loss of about 2% of our data. We were able to detect and correct for this inefficiency during the analysis.

The data used in the cross section calculations were selected from events which were accompanied by a TRIG output. However, events with no TRIG output were also analyzed so that a correction could be applied for the trigger counter deadtime which, at the rates used for data taking, was typically 1 to 3%. The TA pulse-height spectra for the events with no TRIG output are shown in Fig. 10. The raw data spectrum is heavily contaminated with background, whereas selection of good event patterns only revealed a clearly visible electron peak. The good events with TA pulse heights within the expected region of the electron peak were selected to provide the required correction factor.

Thus from a study of the signature of the events in the hodoscopes we were able to assign locations in the θ-p array for the good events and to calculate correction factors to allow for the ambiguous events, for counter inefficiencies, and for the deadtime of the fast trigger counter system. (See Section III.4)

III.3 Radiative Corrections

In Fig. 11 we show the distribution of the selected events on a plane defined by the θ- and p-hodoscope arrays. The peak corresponding to the elastic electron-proton scattering events can be seen clearly on the θ-p plane, together with the radiative tail which extends to lower values of momentum. The counts above the elastic peak are kinematically forbidden for elastic e-p scattering, and can be attributed to scattering in the walls of the target cell or to misdirected electrons which rescattered from the apertures in the spectrometer. The data from the θ-p plane were summed onto a one-dimensional plot of missing

energy. This was defined with respect to the energy for elastic e-p scattering for each θ-interval on the plane, and allowed for the energy loss in the target and windows. The elastic peak should have been at the zero value of missing energy, although it was generally displaced by about 5 MeV, corresponding to a difference in the momentum calibrations of the spectrometer and beam switchyard of less than 0.15%.

The number of counts in each $(\theta_i p_j)$ bin was divided by the solid angle $\Delta\Omega_{ij}$ (see Section IV.1) for that bin. The ordinate or the missing-energy plot was then proportional to the doubly-differential cross section $(d^2\sigma/d\Omega\, dp)$, as shown in Fig. 12.

The radiative degradation of the elastic peak had two sources:

1) The emission of radiation during the actual scattering process.

2) Bremsstrahlung by the incident and scattered electrons resulting in straggling in the target material.

The loss of electron energy from these radiative processes caused some elastically scattered electrons to fall outside the momentum acceptance of the spectrometer. The fraction of events detected depended upon the kinematic variables, the resolution function of the equipment, the amount of material in the flight-path of the incident and scattered electrons, and the missing energy inverval ΔE used.

The data from dummy-target runs, after suitable normalization, was subtracted from the θ-p plane data for full target runs prior to the application of any radiative corrections. In Fig. 13 we indicate the region "C" of the θ-plane which was used for the cross section

calculations. The region "A", corresponding to momenta exceeding the values for elastic e-p scattering, was not used. Any events in this region represented errors in the dummy target subtraction procedure, or a small amount of poletip or aperture scattering in the spectrometer. The boundary between regions "B" and "C" was chosen so as to reject any events from inelastic scattering. To test for edge-effects in the hodoscopes, the events in the outer 2, 4 or 6 θ- and p-hodoscope counters were removed from region "C", and the cross section calculations repeated. Although the results were consistent with each other within the statistical accuracy of the data, we decided to remove the data from the 2 outer counters in the final analysis.

The simplest way to correct the data for radiative losses was to use an integral correction method. A cut was applied to the data at a point ΔE below the momentum of the elastic peak, and then all the events above this cut were summed. Thus, we define:

$$n(\Delta E) = \sum_{\text{region "C"}} \frac{d^2n}{d\Omega dp} \cdot \Delta p \qquad (14)$$

The average cross section can be related to this quantity $n(\Delta E)$ by including the terms due to radiative losses:

$$\left\langle \frac{dn}{d\Omega} \right\rangle = \left[e^{-\delta_R}\right] \left[\frac{e^{-\delta_s}}{1 + 1.107(t_b + t_a)}\right] R(\Delta E) \cdot n(\Delta E) \qquad (15)$$

The factor δ_R allowed for the radiative losses during the scattering process. The formula for δ_R for the case in which only the electron is detected has been reported by Tsai[24] and Meister and Yennie[25]. We

used both formulae, assuming exponentiation of δ_R, and found differences between values of $e^{-\delta_R}$ of about 0.5%. For consistency, we have used the formula due to Tsai[24] for the final data values. The quantity $\exp(-\delta_R)$ was typically between 1.20 and 1.40 in these measurements. The term in parentheses in Eq. (15) corrected for straggling in the target material. In this term,

$$\delta_s = -\frac{4}{3} t_b \ln\left(\frac{E_o}{\eta^2 \Delta E}\right) - \frac{4}{3} t_a \ln\left(\frac{E_o}{\eta \Delta E}\right) \tag{16}$$

where

$$\eta = 1 + \frac{2E_o}{M} \sin^2 \frac{\theta}{2}$$

and $t_b(t_a)$ is the total amount of material in radiation lengths before the center of the target (after the center of the target) in the path of an average incident (scattered) electron. For the denominator of the term in parenthesis in Eq. (15), we used the formula due to Eyges[26] in which the free parameter was chosen to fit the shape of the bremsstrahlung spectrum at low photon energies. The addition of this parameter changed the final cross section by about 0.7%. The correction for straggling varied between 1.10 and 1.30. The factor $R(\Delta E)$ in Eq. (15) corrected for the effect that the emission of photons changed slightly the effective incident energy in the interaction:

$$R(\Delta E) = \left[1 - \frac{e^{-\delta}}{\varepsilon} \eta^2 \chi(q^2, t_b) \left| \frac{\partial}{\partial E_o} \left(\frac{d\sigma}{d\Omega}\right) \right| \left(\frac{d\sigma}{d\Omega}\right)^{-1} \Delta E \right] \tag{17}$$

where

$$\varkappa(q^2,t_b) = \frac{2e^2}{\pi}\left[\ln\left(\frac{q^2}{m_e^2}\right) - 1 + \frac{8t_b}{3}\right]$$

and m_e is the mass of the electron, and e^2 is the fine structure constant. The term $e^{-\delta}$ in Eq. (17) stands for the product of the first two terms on the right hand side of Eq. (15). For calculational convenience the dipole cross section was used in the evaluation of

$$\left|\frac{\partial}{\partial E_o}\left(\frac{d\sigma}{d\Omega}\right)\right|\left(\frac{d\sigma}{d\Omega}\right)^{-1}.$$

In spite of the rapid variation of cross sections the $R(\Delta E)$ correction was typically 0.5%.

When the width of the electron peak became significant compared with the interval ΔE, then the effect of the resolution shape of the peak was included. This was accomplished in the calculation of the term δ_R, which was an average value calculated over the shape of the peak. The integral calculation of $< dn/d\Omega >$ was performed for different values of ΔE as shown in Fig. 14, from which the final result can be seen to be independent of ΔE over quite a large interval.

The radiative corrections were also applied to the data using a differential unfolding scheme.[27] The bin at the highest momentum end of the missing-energy spectrum in Fig. 12 was chosen to be just above the region for elastic electron-proton scattering. Thus, there was no contamination in this bin due to the radiative tail from bins at higher momentum. The counts in this bin were increased to allow for

the radiative losses by applying a correction similar in form to Eq. (15), where the value for ΔE is the half-width of the missing-energy bin size. The number of counts added to the first bin were then used to compute subtractions from all bins at lower momenta using the exact shape of the radiative tail. The second bin was then corrected for radiative losses, and its radiative tail subtracted from the bins at lower momenta. This procedure was repeated for each bin in the missing-energy plot until the final distribution of events corresponded to elastic e-p scattering with no radiative losses. Figure 15 shows the result of this procedure. The raw data are shown as a solid line and the unfolded data as a dashed line. Beyond bin 14 the errors in the ordinates of the corrected data were comparable to the ordinate values, and the fluctuations about zero arose from the statistical fluctuations in the data. Care had to be taken with the propagation of errors in this treatment of the data. The value $< dn/d\Omega >$ was then obtained from a sum of the radiatively-corrected spectrum. The shape of the corrected spectrum represents the resolution function of the equipment. In principle one should generate a missing-energy histogram for each of the 54 θ-bins to allow for the variation of the resolution function in the θ-p plane. However, this was not possible for the runs at lower statistical accuracy. It was performed for a few high statistics runs and the cross section results were within 0.5% of the value obtained using a single missing-energy spectrum.

The application of radiative corrections by the two different techniques (integral and differential) provided a useful check on the accuracy of the methods. When treating the same input data, the resulting

cross section values agreed to within about 1.0%, and thus we assign a relative error of this amount as a consequence of the digital techniques of performing the radiative corrections. By comparing the two methods over a wide range of q^2 values, and from studies of the variation in the predictions of the different theoretical formulae[24,25] for δ_R, we estimate that the radiative corrections produce an absolute uncertainty of up to ±1.5% in the final cross section values.

A small correction factor was applied to $\langle dn/d\Omega \rangle$ to allow for the rapid variation of cross section across the detectors. The large number of events at small angles made the effective scattering angle smaller than the spectrometer angle. This effect was calculated (assuming the Rosenbluth variation of cross section and using the dipole expression for the proton form factors) and the cross section values were reduced about 0.5% to correspond to measurements taken at the exact angle of the central ray of the spectrometer.

III.4 Calculation of Cross Sections and Errors

The cross section values were calculated from

$$\frac{d\sigma}{d\Omega} = \frac{\sum_i C_i}{N_e N_p} \left\langle \frac{dn}{d\Omega} \right\rangle \qquad (18)$$

where:

$\langle dn/d\Omega \rangle$ is the average of the number of counts per sterdian, calculated from the good events on the θ-p plane (see Section III.3) after subtraction of dummy target yields (typically 2 to 4%), and after correction for radiative losses.

N_e is the number of electrons incident to the target, obtained from the toroid charge monitor which had an absolute gain of 1.000.

N_p is the number of protons/cm^2 in the liquid hydrogen target. The target length was known to better than 0.3% and a hydrogen density of 0.07035 g/cm^3 was used. It was not necessary to correct for target heating by the beam, for reasons described below (see Section IV.2).

$\pi_i C_i$ is a multiplication of several correction factors to allow for:

a) Events lost due to the deadtime of the fast trigger system.

b) Events lost by adjacent inefficient hodoscope counters.

c) Electron events which had ambiguous hodoscope patterns and for which θ-p assignments could not be made.

d) The computer (data reading) deadtime as calculated from the kill circuit scalers.

e) Losses due to infrequent magnetic tape logging or reading errors.

The efficiency of the total absorption shower counter for detecting electrons was assumed to be 100%.

In Table IV we list the factors which directly affected the cross section values. Their contributions are shown for a typical data run. The uncertainties in these factors have been separated into those which were relative (random) errors and those which were overall normalization errors. The relative errors mainly arose from counting statistics, empty-target subtraction, relative density of the hydrogen target (±1.0%), uncertainties in the radiative corrections (±1.0%), fluctuation in beam-current monitoring (±0.5%) and uncertainty in the spectrometer solid

angle (±0.5%).

The overall normalization error in our data was estimated to be ±4.0%. This included the uncertainty in the absolute solid angle (±3.0%) (see Section IV.1 for further details), the density of the liquid hydrogen (±1.5%), the lack of the accuracy of the radiative corrections (±1.5%), uncertainty in the procedure for event selection (±1.0%), calibration of the incident energy and scattering angle (±0.8%), beam-current monitor normalization (±0.5%), and target length (±0.3%).

IV. SPECIAL TEST RUNS

Before presenting final results, we will mention some special test runs which were performed to clarify certain aspects of the data.

IV.1 Test of the Optics of the Spectrometer

The optics of the 8-GeV/c spectrometer were designed using the TRANSPORT computer program developed at SLAC[28]. This program used first- and second-order matrix algebra formalism and produced a transformation equation relating the output coordinates of a particle trajectory at the focal planes to the input variables. We define our variables in a right-handed coordinate system. The variables x, θ, y, Φ, δ are measured with respect to the central trajectory of the spectrometer. Thus, x measures deviations from the central trajectory in the horizontal plane, y measures deviations from the central trajectory in the vertical plane, and z measures distances from the target center along the direction of the central trajectory of the spectrometer. The horizontal angle is $\theta = dx/dz$ (note that here θ is not the scattering

angle of the electron), the vertical angle is $\Phi = dy/dz$, and the fractional deviation of the momentum is $\delta = \frac{p - p_o}{p_o}$. TRANSPORT is based on the approximations $\tan\theta \cong \theta$ and $\tan\Phi \cong \Phi$, sometimes called the paraxial approximation. Variables evaluated at the target position are denoted with a "o" subscript. Note that δ and δ_o are the same.

The final optics of the spectrometer was calibrated with the SLAC electron beam. The spectrometer was set at zero degrees and an electron beam of a prescribed energy was transmitted through a system of three small bending magnets and into the spectrometer. The three-magnet system was designed to steer the beam to different horizontal entrance displacements (x_o) and to prescribed horizontal and vertical entrance angles (θ_o and Φ_o). Zinc-sulphide-coated screens, appropriately placed along the beam line near the focal position of the spectrometer, were used to measure the position of the beam as it was transmitted through the spectrometer. The spectrometer was set to several slightly different momenta and the measurements repeated. From these measurements the optics of the system was checked and the various first- and second-order optics matrix elements and the solid angle acceptances were calculated. This program of measurements was made for incident beam momenta of 3, 6, 8 and 9 GeV/c.

In Table V we list the first- and second-order matrix elements as measured for the spectrometer set at a momentum of 8 GeV/c. We have not been able to get detailed agreement between the measured parameters, and the theoretical parameters calculated using TRANSPORT and the magnetic properties of each individual magnet as measured prior to installation in the spectrometer. We suspect that differences arise

from fringe-field effects between magnets due to their proximity to one another, and from the presence of the nearby steel of the spectrometer carriage. A TRANSPORT model in which we adjust the magnet properties of the quadrupoles from the magnetically measured values by a few percent, however, reproduces satisfactorily the observed matrix elements. In addition, as noted below, this same model, when used with a Monte Carlo ray-tracing program, reproduces the measured solid-angle acceptance. The matrix elements varied slightly with the spectrometer momentum. The TRANSPORT model accounts for this momentum dependence by allowing the quadrupole magnet properties also to be slightly momentum dependent. Table VI summarizes the momentum dependence for some of the first-order matrix elements.

The solid angle of the spectrometer was defined by a number of flanges and the sides of some of the vacuum boxes. A computer program was used to calculate the solid angle ($\Delta\Omega_{ij}$) for each θ_i and p_j bin in the hodoscopes. The program used the optics coefficients provided by the TRANSPORT model mentioned above and, using accurate information concerning the shapes and dimensions of the apertures in the spectrometer, traced rays from the target to the detector region. In this manner, an integration was performed over the angular acceptance of the (ij)th bin and over the length of the target.

Part of the optics test was devoted to mapping out the envelope of acceptance of the θ-p plane for given incident beam values of x_o and δ_o. Thirteen different values of x_o and δ_o were chosen, and the incident beam direction (θ_o, ϕ_o) was varied until the beam spot disappeared at the focal planes. A few examples of these measured accept-

ance plots are shown in Fig. 16. These shapes were also calculated with the solid-angle program and the results shown as the solid curves in Fig. 16. The agreement is extremely good and provides an indication of the level of accuracy which can be expected from the solid-angle calculations.

The solid angle can be defined quite accurately by using slits in front of the spectrometer to reduce the vertical angle acceptance ($\pm\Delta\Phi_o$) from the target. For values $\Delta\Phi_o$ less than 15 milliradians, the solid angle was, in principle, completely determined by the slits. Test runs were performed in which the variation of elastic electron-proton scattering cross sections was measured for several slit settings. As long as the solid angle was limited by slits, and not by the vacuum chamber inside the spectrometer, the measured cross sections showed no dependence on slit settings. However, when the slits were opened and the solid angle was limited by the aperture stops within the spectrometer, we measured cross sections which were about six percent larger than those obtained with partially closed slits. It is difficult to design slits so that no "edge effects" are present. For example, the empty-target subtractions for the data at small slit settings did not cleanly subtract from the full-target data. At some values of q^2 in this experiment, cross sections were measured for both open slits and partially closed slits. At other values of q^2, the data were for open slits only. We could devise no way to tell whether cross sections measured with open slits were 6% too high or whether cross sections measured with partially closed slits were 6% too low. In the final analysis we averaged cross sections for those values of q^2 at which data existed for both slit

configurations. For those values of q^2 at which the data were for open slits only, we multiplied the experimental cross sections by a solid-angle correction factor whose magnitude was 0.97. As a result of these data we have assigned an uncertainty of ±3.0% to the absolute value of the solid angle of the spectrometer.

IV.2 Target Heating Tests

Tests were performed to determine the extent of density changes in the liquid hydrogen caused by the high-intensity electron beam. The density changes were monitored by measuring the differences in the count rates from the target as we varied parameters such as beam spot-size at the target, beam-pulse repetition rate and beam intensity. A density change of about 7% results from raising the temperature of the liquid hydrogen in the target cell to its boiling point. The tests revealed that for extremely small beam-spot sizes (about 1 mm in diameter) and for average beam currents near 10μA it was possible to induce density changes of up to 20%. To be certain of keeping density changes below 1% during the data taking we maintained fairly large spot sizes (3 mm side vertically by 6 mm wide horizontally) and generally ran at average currents near 1μA.

For the data at q^2 values greater than $3(\text{GeV}/c)^2$ the counting rates became so low that we preferred to raise the beam current to about 10μA. To check for beam heating effects in these data, we repeated the data runs at lower values of average intensity (obtained by reducing the pulse repetition rate from the accelerator) which we knew from prior tests did not cause beam-dependent hydrogen density changes. Although

as noted above, we could produce a density change when running with extremely small beam spots at high repetition rates, we found that when we ran with fairly large spot sizes and varied the pulse repetition rates we could find no evidence for target heating effects in these data. Further discussion of this point may be found in the thesis of P. N. Kirk[5].

V. RESULTS OF THE EXPERIMENT

In Table VII, we list the final elastic electron-proton scattering cross section values. Only the relative errors are shown. We estimate the normalization uncertainty in our measurements to be ±4%. Table VII also contains the ratio of the cross sections to the "dipole" cross section values. The dipole cross section formula assumes the Rosenbluth formula, the dipole model for the magnetic form factor of the proton and the form factor scaling relation, $G_{EP} = \frac{G_{MP}}{\mu}$. These cross section ratios are plotted in Fig. 17 along with the published electron-proton elastic scattering cross sections from other laboratories[29] for $q^2 > 0.8(\text{GeV/c})^2$. There is reasonable agreement between the measurements from different laboratories.

Table VII contains the values of G_{MP}^S/μ calculated at each q^2 value using the Rosenbluth formula and assuming form factor scaling. As mentioned earlier, the experimental validity of form factor scaling is still open to question[3,5,9] in the region of q^2 below $4(\text{GeV/c})^2$. Thus, there is no satisfactory way to estimate the uncertainty in G_{MP} from a violation of the form factor scaling law at higher q^2 values. If $G_{EP} = 0$, then the values of G_{MP}/μ in Table VII would increase by 4.2%

at $q^2 = 5(\mathrm{GeV}/c)^2$, and by 1.1% at $q^2 = 20(\mathrm{GeV}/c)^2$.

In Fig. 18 we plot the quantity $(G_{MP}^S/\mu)(1 + q^2/0.71)^2$ versus q^2, which indicates there exists a statistically significant deviation from the dipole formula. The figure shows that $G_{MP}^S(q^2)$ may be dropping faster than $1/q^4$ at high q^2.

VI. COMPARISON WITH THEORETICAL MODELS

In recent years there has been an increasing number of theoretical models for the form factors of the nucleon, of widely differing functional forms.

In this section we compare our experimental results for $G_{EP}^S(q^2) = G_{MP}^S(q^2)/\mu$ with the predictions of various models. Table VIII summarizes the chi-square values for the models, and Figs. 19, 20, and 21 show how some of the models agree with our data. The experimental error bars do not include the 4% normalization error in our measurements. For convenience, the comparison of the measurements and theory are made with respect to the "dipole" model. Thus, the solid line at 1.00 on the ordinate of Figs. 19, 20, and 21 represents the dipole prediction. Clearly, this is statistically inconsistent with the data, which tend to fall of faster than $1/q^4$ at high q^2. Statistical adjustment of the coefficient of q^2 in the dipole model to give a best fit with our data yields

$$\frac{G_{MP}^D(q^2)}{\mu} = \frac{1}{(1 + q^2/0.710)^2}$$

VI.1 Connection with Proton-Proton Scattering

In 1964, Orear[30] observed that the differential cross section for elastic proton-proton scattering decreased rapidly for large angles in the center-of-mass system, according to:

$$\left(\frac{d\sigma}{d\Omega}\right)_{\substack{pp \to pp \\ \text{large } \theta}} \propto \exp(-p_\perp/0.15) \qquad (19)$$

where $p_\perp$ is the transverse momentum transfer in GeV/c. Wu and Yang[31] suggested that this might be caused by the spatial extent of the proton, and that the rapid decrease reflected the difficulty in accelerating different parts of the proton without breaking it up. On intuitive grounds they argued that the proton cross section should be proportional to the fourth power of the form factor, that the variable q^2 in elastic e-p scattering should correspond to the variable $p_\perp^2$ in elastic p-p scattering, and hence that

$$\frac{G_{MP}(q^2)}{\mu} = x_1 \exp\left[-(q^2)^{\frac{1}{2}}/0.60\right] \qquad (20)$$

the quantity x_1 is an adjustable parameter, and the constant 0.60(GeV/c) is from p-p scattering. This relation is relevant for large q^2 values only, and it is not clear whether the data of this experiment have indeed reached the asymptotic region. Equation (2), with $x_1 = 0.719$, is shown in Fig. 19.

More recent work by Chou and Yang[32] suggested that if the nucleon is composed of an infinite number of constituent particles, then the front of the nucleon might shield the rear during an interaction. Chou and Yang derived an expression for the form factors which contains an

infinite series in which each term involves some power of the infinite-energy proton-proton scattering amplitude. There is only one free parameter, which is the normalization constant. The first term in the series corresponds to the previous Wu and Yang result. In Fig. 19 we show the fit of the leading terms in their expression,

$$\left[\frac{G_{MP}(q^2)}{\mu}\right]^2 = 0.79\ \exp(-6.50\ q^2) + 0.1999\ \exp(-2.07\ q^2) + 0.01\ \exp(-0.779\ q^2) + 0.0001\ \exp(-0.227\ q^2) \quad (21)$$

which is in better agreement with the data.

Further investigation of the Wu-Yang conjecture has revealed that the exponential decrease is the most rapid decrease permitted for asymptotic form factors[33]. Measuring the form factors in this region is one way to distinguish whether the proton is an infinitely composite particle or has finite composition[34]. Amati and collaborators[35] have shown that the persistence of the dipole behavior into the asymptotic region would favor the finitely composite model. The more composite the particle the more rapidly its form factors decrease toward the limiting exponential.

Pinsky and Trefil[36] predicted an asymptotic model for the proton form factors on the basis of Regge cuts:

$$\frac{G_{MP}(q^2)}{\mu} = x_1\ q^2\ \exp\left[-x_2(q^2)^{\frac{1}{2}}\right] \quad (22)$$

The values $x_1 = 0.288(\text{GeV/c})^{-2}$ and $x_2 = 1.333(\text{GeV/c})^{-1}$ provide the best fit to the data. The general shape does not provide a good fit to the data.

Similarly a model due to Greco[37] based on p-p scattering data has the form

$$\frac{G_{MP}(q^2)}{\mu} = x_1 \exp\left[-(q^2)^{\frac{1}{2}}/1.088\right] \tag{23}$$

It gives a bad fit to our data, but the q^2 behavior is similar to the observed behavior at large q^2.

Drell, Finn and Goldhaber[38] calculated the asymptotic behavior of the form factors for a finitely composite system. Their non-relativistic model led to an exponential decrease in the form factors with a fractional power of q^2 in the exponent:

$$\frac{G_{MP}(q^2)}{\mu} = x_1 P(q^2) \exp\left[-(q^2/x_2^2)^{N/2(N+1)}\right] \tag{24}$$

where N is an integer greater than zero and $P(q^2)$ represents a polynomial in $1/q$, or an oscillatory factor in q, or a product of both. A simple form of Eq. (24), as shown in Fig. 19, is:

$$\frac{G_{MP}(q^2)}{\mu} = x_1 \exp\left[-(q/x_2)^{\frac{1}{2}}\right] \tag{25}$$

where the parameters for a best fit are $x_1 = 22.5$ and $x_2 = 0.042$ GeV/c respectively.

The model of Fried and Gaisser[39] fits the data well at the values of q^2 of this experiment. In their model, the rapid decrease in the p-p scattering is due to the exchange of virtual "soft" neutral vector mesons. This leads to an expression of the form:

$$G_{MP}(q^2)/\mu = H(q^2) \exp\left[x_1 F(q^2)\right] \tag{26}$$

where $F(q^2)$ represents the "soft" part of the exchange, and is given by:

$$F(q^2) = 1 - \frac{(2\tau + 1)}{[\tau(\tau + 1)]^{\frac{1}{2}}} \ln \left[(\tau)^{\frac{1}{2}} + (\tau + 1)^{\frac{1}{2}}\right] \qquad (27)$$

where $\tau = q^2/4M^2$, and M is the proton rest mass. The quantity $H(q^2)$ in Eq. (26) represents the exchange of the "hard" neutral vector mesons. It cannot be calculated in the context of this model, but is assumed to be of the form:

$$H(q^2) = (1 + q^2/x_2)^{-1} \qquad (28)$$

In Eqs. (26) and (28), the parameters for a best fit are $x_1 = 1.364$ and $x_2 = 0.371(\text{GeV/c})^2$ and the curve is shown in Fig. 19.

VI.2 Vector Meson Exchange

Several models of the proton form factors are interpreted in terms of the exchange of vector mesons. Pole-fits were first derived from the dispersion relation which, for spectral functions having negligible widths, can be simply expressed as

$$G_{MP}(q^2)/\mu = \sum_i \frac{x_i}{(1 + q^2/m_i^2)} \qquad (29)$$

where the summation includes all the resonances and m_i is the mass of the i^{th} resonance. For the ρ^o, ω^o, and Φ^o meson resonances, if one assumes zero widths, one can write the simplest 3-pole relation as:

$$G_{MP}(q^2)/\mu = x_1\left[1 + q^2/(0.76)^2\right]^{-1} + x_2\left[1 + q^2/(0.78)^2\right]^{-1}$$
$$+ (1 - x_1 - x_2)\left[1 + q^2/(1.02)^2\right]^{-1} \qquad (30)$$

If one postulates an additional vector meson of mass x_4, then a simple 4-pole model would be:

$$G_{MP}(q^2)/\mu = x_1\left[1 + q^2/(0.76)^2\right]^{-1} + x_2\left[1 + q^2/(0.78)^2\right]^{-1}$$
$$+ x_3\left[1 + q^2/(1.02)^2\right]^{-1} + (1 - x_1 - x_2 - x_3)\left[1 + q^2/x_4^2\right]^{-1}. \qquad (31)$$

The x_i's are free parameters, and the expressions are chosen to constrain the fit so that $G_{MP}/\mu = 1$ at $q^2 = 0$. As seen in Fig. 20 these pole-fits are rather poor fits to the data. The 3-pole fit has best fit values of $x_1 = 5.375$ and $x_2 = -3.330$; the 4-pole fit has $x_1 = 8.8842$, $x_2 = -7.381$, $x_3 = 1.005$ and $x_4^2 = 1.141(\text{GeV/c})^2$. The expressions in Eqs. (30) and (31) can only be applied to the proton form factor. Attempts have been made to express pole-fits so that they can be applied to both the neutron and proton form factor data, but the fits[40] were poor for q^2 values about $1(\text{GeV/c})^2$.

Wataghin[41] obtained a better fit, shown in Fig. 20, by introducing finite widths for the resonances:

$$G_{MP}(q^2)/\mu = \sum_i x_i \left[-q^2 - m_i^2 + \gamma_i (q_i^2 + q^2)^{\frac{1}{2}}\right]^{-1} \qquad (32)$$

where the m_i's and γ_i's are the masses and widths of the ρ^o, ω^o, and Φ^o mesons respectively, the q_i's are equal to $(0.28)^2$, $(0.42)^2$, and $(0.99)^2$, respectively, and x_1 and x_2 are free parameters and

$x_3 = 1 - x_1 - x_2$. The three terms in Eq. (32) combine to produce a rapid decrease in the form factor G_{MP}.

Kreps and Moffat[42] derived a formula which involves no free parameters:

$$G_{MP}(q^2)/\mu = \frac{1}{2}\left\{\frac{1 + \mu_n/\mu_p}{\left[1 + q^2/m_\omega^2\right]\left[1 + q^2/m_\phi^2\right]} + \frac{1 - \mu_n/\mu_p}{\left[1 + q^2/m_\rho^2\right]^2}\right\} \qquad (33)$$

where μ_n, μ_p are the magnetic moments of the neutron and proton, respectively. This formula assumes the dipole structure for the ρ-meson, and Krepps and Moffat suggest that the ρ might possible show a double-peaked missing-mass spectrum in an experiment with sufficiently fine resolution. Eq. (33) fits our data poorly.

Meyer[43] developed a hybrid model in which the form factor is given by the product of two terms:

$$\frac{G_{MP}(q^2)}{\mu} = F(q^2)\left[1 + q^2/(0.78)^2\right]^{-1}. \qquad (34)$$

The function $F(q^2)$ is derived from non-relativistic quantum mechanics under the assumption of Fermi statistics for the quarks in the nucleon, where

$$F(q^2) = \frac{32}{5(y + 2)^8}\left(19y^4 + 48y^3 + 88y^2 + 80y + 40\right) \qquad (35)$$

and

$$y = \left(1 + 2\,q^2/3x_1\right)^{\frac{1}{2}} - 1 \qquad (36)$$

Meyer's fit involves one free parameter, x_1, and the best fit value (as shown in Fig. 20) is $0.531(\text{GeV}/c)^2$.

The work of Veneziano[44] has led to several new and interesting models for the proton form factors. These models assume that there exists an infinite number of zero-width vector mesons lying on a family of linearly rising Regge trajectories. The family includes one parent trajectory, denoted by $\alpha(q^2)$, and an infinite sequence of daughter trajectories whose intercepts at $q^2 = 0$ are given by $\alpha(0) - n$, where n is a different positive integer for each daughter trajectory. The daughter trajectories are assumed to have the same slope as the parent. These models predict Regge recurrences of the vector mesons, which have so far not been observed.

To account for all these vector resonances, DiVecchia and Drago[45], and also Frampton[46], wrote

$$\frac{G_{MP}(q^2)}{\mu} = \frac{\Gamma[1 - \alpha(q^2)]}{\Gamma[1 - \alpha(0)]} \frac{\Gamma[c - \alpha(0)]}{\Gamma[c - \alpha(q^2)]} \tag{37}$$

which is normalized to unity at $q^2 = 0$. In both models, the trajectory is assumed to be a linear function of q^2:

$$\alpha(q^2) = a - bq^2 \tag{38}$$

DiVecchia and Drago chose $a = 0.5$ and $b = 0.854(\text{GeV}/c)^{-2}$, while Frampton used $a = 0.5$ and $b = 1.00(\text{GeV}/c)^{-2}$. The constant c in Eq. (37) was a free parameter in Frampton's model with a best fit value of 3.27. DiVecchia and Drago set c to 3.5 by requiring that the first zero in $G_{MP}(q^2)/\mu$ occur at the (timelike) value of $q^2 = -4M^2$, where M is the nucleon mass. The curve for Frampton's model is shown in Fig. 20.

Jengo and Remiddi[47] produced a Veneziano-type form factor of the form:

$$\frac{G_{MP}(q^2)}{\mu} = \frac{\Gamma\left[1 - \alpha(q^2)\right]}{\Gamma\left[1 - \alpha(0)\right]} \sum_{n=1}^{3} x_n \frac{\Gamma\left[1.5 + n - \alpha(0)\right]}{\Gamma\left[1.5 + n - \alpha(q^2)\right]} \qquad (39)$$

where x_1 and x_2 are adjustable parameters, and $x_3 = 1 - x_1 - x_2$ in order to ensure the proper normalization for $G_{MP}(0)/\mu$. They assumed a linear trajectory with $a = 0.483$ and $b = 0.885(\text{GeV/c})^{-2}$. The best fit to the data gives $x_1 = 1.050$, $x_2 = 0.503$.

VI.3 Other Models

Since the form factors are the Fourier transforms in the Breit frame of the spatial distributions of charge and magnetism[48], and since the presence of dips[49] in the charge form factors of ^{4}He and other nuclei may be accounted for by a rather small flattening out of the charge density near the center of the nucleus, Morpurgo[50] speculated that the charge density $\rho(r)$ of the proton might also exhibit such a depression and suggested a form of $\rho(r)$ which was the difference between two exponentials. From this expression, the Fourier transform became:

$$G_{EP}(q^2) = \frac{1}{(a^3 - \alpha r_o^3)} \left[\frac{a^3}{(1 + a^2q^2)^2} - \frac{\alpha r_o^3}{(1 + r_o^2q^2)^2}\right] \qquad (40)$$

If $\alpha = 0$, then Eq. (4) reduces to a dipole form factor. In Fig. 21 we have drawn the best fit value of Morpurgo's form factor which assumes $G_{MP}(q^2)/\mu = G_{EP}(q^2)$ and uses $a^2 = 1.141(\text{GeV/c})^{-2}$ and has the fitted values $\alpha = 0.657$ and $r_o = 0.096(\text{GeV/c})^{-1}$.

Figure 21 also contains a fit to a model by Green and Ueda[51]

which was derived from their work on one-boson-exchange potentials:

$$G_{MP}(q^2)/\mu = \left[(1 + q^2/x_1)\ (1 + q^2/x_2)\ (1 + q^2/x_3)\right]^{-1} \qquad (41)$$

The best fit has $x_1 = 0.393(\mathrm{GeV/c})^2$, $x_2 = 1.818(\mathrm{GeV/c})^2$, and $x_3 = 20.31(\mathrm{GeV/c})^2$. The x_i's are semi-phenomenological parameters related to the masses of vector mesons.

The model of Mack[52], based on the statistics of meson emission predicted that as q^2 increased the form factors decreased due to the increasing probability for soft meson emission. This led to an expression which may be rewritten

$$G_{MP}(q^2)/\mu = (1 + q^2/4m_\pi^2)^{-\left[x_1 + x_2 \ln(1 + q^2/4m_\pi^2)\right]} \qquad (42)$$

where x_1 and x_2 are free parameters. In Fig. 21 we show the best fit for which $x_1 = 0.109$ and $x_2 = 0.212$.

Fujimura, Kobayashi, and Namiki[53] considered models taking account of the Lorentz contraction of the nuclear core. The model shown in Fig. 21 had the form

$$\frac{G_{MP}(q^2)}{\mu} = \frac{\exp\left[-x_1 q^2/(1 + 0.568\ q^2)\right]}{(1 + 0.846\ q^2)\ (1 + 0.568\ q^2)} \qquad (43)$$

with a best fit value $x_1 = 0.938(\mathrm{GeV/c})^{-2}$.

In conclusion, for the models mentioned above, we list the fits to our data in Table VIII. The values of the total chi-square and the number of degrees of freedom are noted for each fit. One can see that the model for the magnetic form factor of the proton which has the best fit to our high q^2 data is that due to Fried and Gaisser[39]. However, although there is some success in analytic fitting of the data, we feel that more work is needed before the electromagnetic form factors of the proton are understood at a fundamental level.

ACKNOWLEDGEMENTS

We wish to express our gratitude and appreciation to all the members of the Stanford Linear Accelerator Center.

Particular acknowledgements are due to those who helped build the spectrometer facility under the direction of E. A. Taylor. L. E. Brown, R. R. Cochran, A. J. Cook, W. Davies-White and A. Gallagher were all active in the mechanical design of the magnetic systems and support structures of the spectrometers. M. Berndt was in charge of the large power supplies for the magnets. M. J. Browne, T. J. Lawrence and R. P. Paul provided most of the engineering effort for the instrumentation of the spectrometers. The on-line computer used in the experiment was brought up and maintained by W. L. Graves and N. M. Heinen who were also active in the interfacing of the computer to the experiment. R. M. Brown, M. A. Fisherkeller and A. E. Gromme of the Computer Group at SLAC provided a great deal of effort on the basic systems for the computer.

Our thanks are also due to members of Group "C" and Group "F" at SLAC, who collaborated on the construction of the facility, and to K. L. Brown of SLAC and Charles Peck of C.I.T. for their collaboration on the basic design of the 8-GeV/c spectrometer.

We are grateful for the operation of the accelerator by the Technical Division under the direction of R. B. Neal and for the operation of the accelerator proper under the direction of V. G. Price. We were greatly assisted by the efforts of E. J. Seppi, J. L. Harris and H. A. Weidner in the operation of the beam switchyard. The contribution of the chief operators and the operating crews under the very

trying circumstances of obtaining precision beams from a new accelerator is much appreciated.

We are grateful to Miss E. Campell and Mrs. E. Miller for help with portions of the data analysis and to the M.I.T. Physics Department and Laboratory of Nuclear Science for their support of the M.I.T. collaborators.

Finally, we wish to thank Mrs. Arlene Spurlock for her untiring efforts as secretary to Group "A" at SLAC.

REFERENCES

1. R. Hofstadter and R. W. McAllister, Phys. Rev. 98, 217 (1955).
2. W. Albrecht et al., Phys. Rev. Letters 17, 1192 (1966); and 18, 1014 (1967).
3. W. Bartel et al., Phys. Letters 33B, 245, (1970).
4. J. Litt et al., Phys. Letters 31B, 40 (1970).
5. We now report the final values of our data. Preliminary values from less than 50% of the data were published earlier by D. H. Coward et al., in Phys. Rev. Letters 20, 292 (1968). Additional details may be found in the Ph.D. Thesis of Paul N. Kirk, Massachusetts Institute of Technology, February 1970 (unpublished).
6. M. N. Rosenbluth, Phys. Rev. 79, 615 (1950).
7. R. Hofstadter, Rev. Mod. Phys. 28, 214 (1956).
8. T. Janssens et al., Phys. Rev. 142, 922 (1966).
9. C. Berger et al., Phys. Letters 35B, 87 (1971)., Price et al., Phys. Rev. D4, 45 (1971).
10. R. H. Hofstadter, F. Bumiller and M. R. Yearian, Rev. Mod. Phys. 30, 482 (1958).
11. For a detailed account of the SLAC machine see: The Stanford Two-Mile Accelerator, R. B. Neal, Editor (W. A. Benjamin, Inc. New York, 1968).
12. R. W. Larsen and D. Horelick, A Precision Toroidal Charge Monitor for SLAC, Proceedings of the Symposium on Beam Intensity Measurement, Daresbury Nuclear Physics Laboratory, England, April 23-26, 1968.

13. D. Yount, Nucl. Instr. and Meth. 52, 1 (1967).

14. The method of preparing the most stable monitor of this type is described in E. L. Garwin and N. Dean, Method of Stabilizing High Current Secondary Emission Monitors, Proceedings of the Symposium on Beam Intensity Measurement, Daresbury Nuclear Physics Laboratory, England, April 23-26, (1968).

15. R. L. Anderson, Nucl. Instr. and Meth. 70, 87 (1969).

16. The H_2 vapor pressure thermometers are built at SLAC.

17. Cryogenic Data Book, UCRL 3421 (1956); Hydrogen Handbook AFFTC-TR-60-90 (1960).

18. R. Anderson, D. Gustavson, R. Prepost and D. Ritson, Nucl. Instr. and Meth. 66, 328 (1968).

19. The design concepts are given in a paper by L. Mo and C. Peck, "8-BeV/c Spectrometer", Technical Report No. TN-65-29, Stanford Linear Accelerator Center, Stanford California (1965).

20. SLAC User's Handbook, Section E, Stanford Linear Accelerator Center; and W. K. H. Panofsky, Proceedings of the International Symposium on Electron and Photon Interactions at High Energies, Hamburg, Germany (1965).

21. W. A. Davies-White, "Alignment of 8-BeV Spectrometer," Technical Report No. TN-65-70, Stanford Linear Accelerator (1965); W. K. H. Panofsky and W. F. Marshall "The Use of a Magnetic Pickup as an Alignment Indicator with a Stretched-Wire Technique" and "Proposed Systems and Circuits for Magnetic Alignment Pickups", Technical Report No. TN-65-74, Stanford Linear Accelerator Center (1965).

22. G. Backenstoss et al., Nucl. Instr. and Meth. 21, 155 (1963).

23. A. Boyarski, "The Online Control, Analysis and Display System for the SLAC Multi-GeV Spectrometers", Proceedings of the Conference on Computer Systems in Experimental Physics, Skytop, Penn. (March 1969).

24. Y. S. Tsai, Phys. Rev. 122, 1898 (1961).

25. N. Neister and D. R. Yennie, Phys. Rev. 130, 1210 (1963).

26. L. Eyges, Phys. Rev. 76, 264 (1949). We have used his equation (16) with a = 0.25 and b = 1.333.

27. H. W. Kendall and D. Isabelle, Bull. Am. Phys. Soc. 9, 94, (1964); see also H. Crannell, Nuc. Instr. and Methods 71, 208 (1969).

28. K. L. Brown, Advances in Particle Physics, Vol. I, Cool and Marshak, Editors (Interscience, 1968), p. 71; or, equivalently, Report SLAC-75 Stanford Linear Accelerator Center, Stanford, California (July 1967). The implementation of TRANSPORT on the IBM 360 computer is described by K. L. Brown and S. K. Howry in Report SLAC-91, Stanford Linear Accelerator Center, Stanford, California (July 1970).

29. The data compilation of electron-proton elastic scattering cross sections for $q^2 > 0.8 (\mathrm{GeV}/c)^2$ used in Fig. 17 have been taken from the following papers: BONN: C. Berger et al., Phys. Letters 28B, 276 (1968); Bonn Preprint 1-075 (July 1969) published in abstract form in the Proceedings of the Fourth International Symposium on Electron and Photon Interactions at High Energies, Liverpool,

England, (1969), edited by D. W. Braben and R. E. Rand (Daresbury Nuclear Physics Laboratory, Daresbury, Lancashire England, 1970), p. 276. CEA: M. Goitein et al., Phys. Rev. Letters 18, 1016 (1967.) Cornell: K. Berkelman et al., Phys. Rev. 130, 2061 (1963). DESY (internal beam): H. J. Behrend et al., Nuovo Cimento 48, 140 (1967); W. Albrecht et al., Phys. Rev. Letters 17, 1192 (1966); W. Albrecht et al., Phys. Rev. Letters 18, 1014 (1967). DESY (external beam): W. Bartel et al., Phys. Rev. Letters 17, 608 (1966); Phys. Rev. Letters 25B, 236 (1967). Stanford: T. Janssens et al., Phys. Rev., 142, 922 (1966). Plots similar to that of Fig. 17 may be found in Goitein et al., Phys. Rev. D1, 2449 (1970).

30. J. Orear, Phys. Rev. Letters 12, 112 (1964).

31. T. T. Wu and C. N. Yang, Phys. Rev. 137, B708 (1965).

32. T. Chou and C. N. Yang, (a) Phys. Rev. Letters 20, 1213 (1968) and (b) Phys. Rev. 170, 1591 (1968).

33. A. Martin, Nuovo Cimento 37, 671 (1965); A. M. Jaffe, Phys. Rev. Letters 17, 661 (1966).

34. J. D. Stack, Phys. Rev. 164, 1904 (1967); J. Harte, Phys. Rev. 165, 1557 (1969); J. S. Ball and F. Zachariasen, Phys. Rev. 170, 1541 (1968).

35. D. Amati et al, Phys. Rev. Letters 27B, 38 (1968).

36. S. Pinsky and J. S. Trefil, Phys. Letters 27B, 518 (1968).

37. M. Greco, Phys. Letters 27B, 578 (1968).

38. S. D. Drell, A. C. Finn and M. H. Goldhaber, Phys. Rev. 157, 1402 (1967).

39. H. M. Fried and T. K. Gaisser, Phys. Rev. 179, 1941 (1969).

40. M. Goitein, J. R. Dunning and R. Wilson, Phys. Rev. Letters 18, 1018 (1967).

41. V. Wataghin, Nuovo Cimento 54, 805 (1968); Nuovo Cimento 54, 840 (1968).

42. R. E. Kreps and J. W. Moffat, Phys. Rev. 175, 1942 (1968); Phys. Rev. 175, 1945 (1968).

43. R. F. Meyer, Nuovo Cimento Letters 2, 76 (1969).

44. G. Veneziano, Nuovo Cimento 57, 190 (1968).

45. P. DiVecchia and F. Drago, Nuovo Cimento Letters 1, 917 (1969).

46. P. H. Frampton, Phys. Rev. 186, 1419 (1969).

47. R. Jengo and E. Remiddi, Nuovo Cimento Letters 1, 922 (1969).

48. R. G. Sachs, Phys. Rev. 126, 2256 (1962).

49. R. F. Frosch, J. S. McCarthy, R. Rand, and M. Yearian, Phys. Rev. 160, 874 (1967).

50. G. Morpurgo, Phys. Letters, 27B, 378 (1968).

51. A. E. S. Green and T. Ueda, Phys. Rev. Letters 21, 1499 (1968).

52. G. Mack, Phys. Rev. 154, 1617 (1967).

53. K. Fujimura, T. Kobayashi, and M. Namiki, Progr. Theoret. Phys. 43, 73 (1970).

TABLE CAPTIONS

I. The main parameters of the 8-GeV/c magnetic spectrometer.

II. Specification of the magnet elements of the 8-GeV/c spectrometer. The power requirements listed in the table correspond to excitation of the spectrometer to a momentum of 8 GeV/c.

III. Hodoscope patterns in the θ- or p-arrays in the 8 GeV/c spectrometer (0 = set bits, - = unset bits). The arrows indicate the assigned bin locations. A double arrow means that one or the other arrow was chosen randomly. Type x is any combination of patterns 2, 3, 4 or 5.

IV. The correction factors and error contributions for a typical cross section calculation. As noted in the text, the correction factor listed here for radiative corrections is not typical but is the maximum correction.

V. First- and second-order matrix elements for the 8 GeV/c spectrometer.

VI. The notation is described in the text, Section IV.1. For the first-order matrix elements the upper number is the value measured for p_o = 8 GeV/c. The lower numbers in parentheses, are computed from the TRANSPORT model of the spectrometer. An asterisk denotes that the model was adjusted until the predicted matrix element equaled the measured matrix element. The notation (0^{++}) indicates that the matrix elements are identically zero because in the model there is no possibility, in first order, or mixing the horizontal and vertical planes. The errors are somewhat hard to assess and we have assigned, somewhat arbitrarily, a ±1% error to the p- and θ-dispersions. As an example of the notation, (y/δ_o) = -2.907(cm/%)

means that a particle with momentum 1% greater than the spectrometer setting moves downward by 2.907 cm at the momentum hodoscope. The terms dependent on y_o were not measured. TRANSPORT predicts that $(y/y_o) = -0.928$ (cm/cm).

VI. A comparison between the measured and predicted momentum-dependence of some of the first-order optics coefficients. The values predicted by the TRANSPORT computer program are shown in parentheses. At each momentum the TRANSPORT model was adjusted until the predicted values for the (x/x_o), (x/θ_o) and (y/δ_o) matrix elements equaled the measured values.

VII. Final electron-proton elastic scattering cross sections. Only random errors are shown. There is an overall normalization error, not included here, which we estimate to be ±4%. The G_{MP}^S/μ values are calculated at each q^2 value using the Rosenbluth equation and assuming $G_{EP} = G_{MP}/\mu$. If $G_{EP} = 0$, then the values of G_{MP}/μ would increase by 10.8% at $q^2 = 2(\text{GeV/c})^2$, 4.2% at $q^2 = 5(\text{GeV/c})^2$, and 1.1% at $q^2 = 20(\text{GeV/c})^2$. Eqs. (9) and (10) give the dipole cross section.

VIII. Summaries of the various theoretical fits mentioned in the text.

TABLE I

Maximum Momentum	9.0 GeV/c
Horizontal Beam Position Acceptance	±10 cm
Horizontal Angle (θ) Acceptance	±7.8 mrad
θ Dispersion (at 8 GeV/c)	4.57 cm/mrad
Detector θ Resolution	±0.2 mrad
Vertical Angle (Φ) Acceptance	±29.5 mrad
Solid Angle	0.75 millisteradians
Momentum (p) Acceptance	±2.0% cm/%
p Dispersion (at 8 GeV/c)	2.91 cm/%
Detector p Resolution	±0.05%
Tilt of p-Focal Plane	13.7°
Length from Target to θ-Focal Plane	21.4 m
Separation Between p- and θ-Focal Planes	0.5 m

TABLE II

Element	Pole-Tip Field (kG)	Field Gradient (kG/cm)	Length of Iron (Inches)	Magnet Aperture (Inches)	Power Requirements		
					Current (amps)	Power (kW)	Regulation (%)
Q 81	7.6	0.54	40.00	11.00 dia	1640	126	±0.1
Q 82	11.1	0.57	51.25	15.25 dia.	2350	221	±0.1
Q 83	7.3	0.38	51.25	15.25 dia.	1550	96	±0.1
B 81	19.3	----	136.00	13.755(gap) × 22	2200	880	±0.01
B 82	19.3	----	136.00	13.755(gap) × 22	2200	880	±0.01

TABLE III

Pattern	Description	Example
	Good Codes:	
1	One Bit	----------o-------- ↑
2	2 adjacent	----------oo---- ↑↑
3	3 adjacent	----ooo---------- ↑
4	4 adjacent	----------oooo- ↑↑
5	5 or more adjacent	----------ooooo--- ↑↑
6	One track (type x) + one or more singles	--------o---------oo ↑↑
7	2 singles with one intervening blank	---o-o---------- ↑
	Ambiguous Codes:	
8	2 tracks (type x) + zero or more singles	-oo---------o--ooo--
9	3 or more tracks (type x) + zero or more singles	-oo--oo------ooo-o--
10	Two or more singles (excluding pattern 7)	--o-------o----o----
11	10 or more set bits (frequency < 0.1%)	oooooo-ooooo--o-----
	Bad Codes:	
12	Blank	----------
13	Edge bit (s) only	o----------

TABLE IV

Correction or Error (example)	Correction Factors	Relative Errors %	Normalization Errors %
Current Monitor	1.000	0.5	0.5
Target Length	1.000	0.15	0.3
Target Density	1.000	1.0	1.5
Solid Angle	1.000	0.5	3.0
Incident Energy and Scattering Angle	1.000	0.0	0.8
Variation of Cross Section	0.997	0.0	0.0
Radiative Corrections	1.700	1.0	1.5
Trigger Efficiency	1.010	0.0	0.0
Shower Counter Efficiency	1.000	0.0	0.0
Hodoscope Counter Efficiency	1.010	0.2	0.0
Computer Deadtime	1.020	0.0	0.0
Magnetic Tape Losses	1.005	0.0	0.0
Ambiguous Pattern Contribution	1.030	0.3	0.3
Event Selection Procedure	1.000	0.5	1.0
TOTAL	1.942	1.7	4.0
Counting Statistics	-----	Variable	---

TABLE V

First Order:

	x_o(cm)	θ_o(mrad)	Φ_o(mrad)	δ_o(%)
x(cm)	0.028 (0.028*)	4.575 ± 0.046 (4.575*)	-0.019 (0^{++})	0.027 (0^{++})
θ(mrad)	-0.194 (-0.189)	4.858 (4.893)	-0.020 (0^{++})	0.071 (0^{++})
y(cm)	-0.002 (0^{++})	0.007 (0^{++})	-0.004 (-0.014)	-2.907 ± 0.029 (-2.907*)
Φ(mrad)	-0.008 (0^{++})	0.027 (0^{++})	-1.077 (-1.090)	0.094 (0.203)

Second Order: (only the largest matrix elements are listed)

Matrix Element	(Units)	Measured	Predicted	Meas./Pred.
$(x/x_o\delta_o)$	(cm/cm·%)	0.0433	0.0428	1.012
$(x/\theta_o\delta_o)$	(cm/mrad·%)	-0.0104	-0.0135	0.771
$(\theta/x_o\delta_o)$	(mrad/cm·%)	0.0484	0.0450	1.076
$(\theta/\theta_o\delta_o)$	(mrad/mrad·%)	-0.0236	-0.0282	0.838
$(y/\Phi_o\delta_o)$	(cm/mrad·%)	0.0120	0.0126	0.953
$(\Phi/\delta_o\delta_o)$	(mrad/(%)^2)	-0.0486	-0.0505	0.963

TABLE VI

	Coefficients	p_o, Momentum (GeV/c			
		3.006	6.009	8.005	9.003
Measured Values (fixed)	(x/x_o)(cm/cm)	0.038	0.021	0.028	0.015
	(x/θ_o)(cm/mrad)	4.517	4.547	4.575	4.590
	(y/δ_o)(cm/%)	-2.959	-2.939	-2.907	-2.844
Comparison Values	(θ/θ_o)(mrad/mrad)	4.791 (4.801)	4.825 (4.847)	4.858 (4.894)	4.880 (4.946)
	(y/Φ_o)(cm/mrad)	0.002 (0.006)	-0.001 (-0.006)	-0.004 (-0.014)	-0.005 (-0.139)
	(Φ/Φ_o)(mrad/mrad)	-1.074 (-1.090)	-1.076 (-1.083)	-1.077 (-1.092)	-1.079 (-1.137)

TABLE VII

Four-Momentum Transfer Squared q^2 $(GeV/c)^2$	Incident Beam Energy E_o (GeV)	Electron Scattering Angle θ (deg)	Cross Section $\left(\frac{d\sigma}{d\Omega}\right)$ (cm^2/sr)	$\left(\frac{d\sigma}{d\Omega}\right)\Big/\left(\frac{d\sigma}{d\Omega}\right)_{DIPOLE}$	$\frac{G_{MP}^S}{\mu}$ (Assuming $G_{EP} = G_{MP}/\mu$)
0.999	3.996	15.44	$(0.659 \pm 0.012) \times 10^{-31}$	1.007 ± 0.018	0.1733 ± 0.0016
1.498	6.197	12.15	$(0.3306 \pm 0.0059) \times 10^{-31}$	1.073 ± 0.019	0.1071 ± 0.0010
1.999	6.197	14.40	$(0.829 \pm 0.017) \times 10^{-32}$	1.093 ± 0.022	$(0.718 \pm 0.007) \times 10^{-1}$
2.502	7.909	12.59	$(0.4755 \pm 0.0076) \times 10^{-32}$	1.068 ± 0.017	$(0.5051 \pm 0.0040) \times 10^{-1}$
3.759	9.998	12.45	$(0.948 \pm 0.019) \times 10^{-33}$	1.066 ± 0.021	$(0.2606 \pm 0.0026) \times 10^{-1}$
5.075	10.70	13.99	$(0.1856 \pm 0.0040) \times 10^{-33}$	1.008 ± 0.022	$(0.1513 \pm 0.0016) \times 10^{-1}$
6.270	11.35	15.10	$(0.546 \pm 0.025) \times 10^{-34}$	0.932 ± 0.042	$(0.999 \pm 0.023) \times 10^{-2}$
7.498	12.00	16.07	$(0.1950 \pm 0.0060) \times 10^{-35}$	0.897 ± 0.028	$(0.709 \pm 0.011) \times 10^{-2}$
8.752	12.69	16.85	$(0.713 \pm 0.042) \times 10^{-35}$	0.777 ± 0.046	$(0.496 \pm 0.015) \times 10^{-2}$
9.982	13.33	17.59	$(0.362 \pm 0.014) \times 10^{-35}$	0.838 ± 0.033	$(0.4037 \pm 0.0078) \times 10^{-2}$
12.50	14.66	18.80	$(0.849 \pm 0.061) \times 10^{-36}$	0.722 ± 0.052	$(0.2454 \pm 0.0088) \times 10^{-2}$
15.10	16.06	19.72	$(0.273 \pm 0.028) \times 10^{-36}$	0.695 ± 0.071	$(0.1681 \pm 0.0086) \times 10^{-2}$
20.00	17.31	24.04	$(0.313 \pm 0.061) \times 10^{-37}$	0.62 ± 0.12	$(0.926 \pm 0.090) \times 10^{-3}$
25.03	17.31	35.09	$(0.48 \pm 0.21) \times 10^{-38}$	1.05 ± 0.46	$(0.78 \pm 0.17) \times 10^{-3}$

TABLE VIII

Authors of Model	Ref.	Eq.	Minimum Chi Squared	Degrees of Freedom	Parameter Values Determined by Minimum Chi-Square
Dipole			179	13	Parameter = 0.710
Wu, Yang	31	20	997	13	$x_1 = 0.719$
Chou, Yang	32	21	17.1	10	
Pinsky, Trefil	36	22	>1000	12	$x_1 = 0.288(\text{GeV/c})^{-2}$, $x_2 = 1.333(\text{GeV/c})^{-1}$
Greco	37	23	>1000	13	$x_1 = 0.096$
Drell, Finn, Goldhaber	38	25	32.5	12	$x_1 = 22.54$, $x_2 = 0.042$ GeV/c
Fried, Gaisser	39	26	7.9	12	$x_1 = 1.364$, $x_2 = 0.371(\text{GeV/c})^2$
3-Pole		30	61	12	$x_1 = 5.375$, $x_2 = -3.330$
4-Pole		31	17.6	10	$x_1 = 8.842$, $x_2 = -7.381$, $x_3 = 1.005$, $x_4 = 1.069$ GeV/c
Wataghin	41	32	19.7	12	$x_1 = 0.675$, $x_2 = -2.286$
Kreps, Moffat	42	33	136	14	No adjustable parameters
Meyer	43	34	132	13	$x_1 = 0.531(\text{GeV/c})^2$
DiVecchia, Drago	45	37	228	13	Normalization fit to 0.912 at $q^2 = 0$
Frampton	46	37	41	13	$C = 3.27$
Jengo, Remiddi	47	39	278	12	$x_1 = 1.050$, $x_2 = -0.503$
Morpurgo	50	40	104	11	$\alpha = 0.657$, $r_o = 0.096(\text{GeV/c})^{-1}$
Green, Ueda	51	41	17.2	11	$x_1 = 0.393(\text{GeV/c})^2$, $x_2 = 1.818(\text{GeV/c})^2$, $x_3 = 20.31(\text{GeV/c})^2$
Mack	52	42	16.5	12	$x_1 = 0.109$, $x_2 = 0.212$
Fujimura, et al.	53	43	214	13	$x_1 = 0.938(\text{GeV/c})^{-2}$

FIGURE CAPTIONS

1. Side and top views of the experimental arrangement in End Station A. Details of the components are described in the text.
2. Schematic of the magnetic transport system for the primary electron beam between the end of the accelerator and the liquid hydrogen target in End Station A.
3. Schematic drawing of a typical liquid hydrogen target, approximately to scale.
4. Calculated trajectories through the 8-GeV spectrometer for different values of the initial angles (θ_o and Φ_o) and deviations in momentum (δ).
5. The requirement of 0.1% resolution in the scattered momentum sets requirements on the resolution of the scattering angle, shown in (a) (see Eq. (12)), and on the resolution of the energy of the incident electron beam, shown in (b) (see Eq. (13)).
6. 8-GeV/c Spectrometer Assembly.
7. Top and side views of the counters and apertures inside the detector shielding following the spectrometer.
8. Simplified layout of the fast electronics. C is coincidence, D is discriminator, DCD is discriminator-coincidence-discriminator, LA is linear adder, PS is pulse stretcher. Various reset lines for clearing the appropriate electronics modules just prior to the arrival of the beam pulse are not shown.

9. These semi-log plots illustrate the effect of various cuts on the pulse-height spectrum from the total absorption counter. E = 6.6 GeV and $q^2 = 2.5(\text{GeV}/c)^2$. (a) Raw data as logged on tape. (b) The raw data after the requirement of a pulse from the TA discriminator. (c) The raw data after the requirement of a TRIG signal. (d) The raw data after the requirement of a good code in both the p- and θ-hodoscopes. (e) The spectrum resulting when the three requirements b, c, and d, are applied simultaneously.

10. (a) Starting with the spectrum in Fig. 9a events were selected which had no TRIG pulse. (b) Then good codes in both the p- and θ-hodoscopes were required. The resulting TA pulse height spectrum is characteristic of good electron events and gives a measure of the dead time in the TRIG circuits.

11. A drawing made from a photograph of an on-line two-dimensional display showing the number of counts in the θ-p plane. The extent in the θ-p plane represents one setting of the spectrometer. The elastic peak is clearly seen. The peak height increases toward smaller θ. The radiative tail extends toward lower p.

12. An elastic scattering peak plotted in terms of missing energy, the difference between the secondary energy expected at the observed angle assuming no radiation and the actually observed energy. No radiative corrections have been made. ΔE represents approximately the momentum acceptance of the equipment.

13. Schematic drawing of the θ-p plane showing the region of the elastic peak. Region A, above the elastic peak and kinematically forbidden, was not used. Region C contained many of the radiatively degraded electrons and was used in calculating the cross section. Region C was made as large as possible, and the boundary between regions B and C was chosen to reject events from inelastic scattering. In Figs. 12 and 14 ΔE is the energy between the elastic peak and the boundary between regions B and C.

14. The result of the integral radiative correction according to Eq. (15) is shown as a function of the energy interval ΔE included below the elastic peak.

15. The result of the differential radiative correction in which the measured spectrum, the solid line, is corrected bin by bin to give the corrected spectrum, the dashed line, whose width illustrates the overall resolution of the experiment. Each missing energy bin is 6.57 MeV.

16. Results of optics tests in which the primary electron beam was directed up the spectrometer. For each graph the parameters x_o and δ were fixed. Then the angles θ_o and Φ_o were varied until the beam just vanished on fluorescent screens near the focal planes of the spectrometer. Each point represents such a measurement. The solid curves are the corresponding result of the ray-tracing program used to calculate the the solid angle acceptance as discussed in the text.

17. Some of the world data for elastic e-p scattering divided by the dipole cross section (Eqs. (9) and (10)). The errors in the points from the present experiment, shown as solid dots, do not include the estimated overall normalization error of ±4%. There is reasonably good agreement between laboratories, and there are deviations from the dipole cross sections.

18. The quantity $(G_{MP}^S/\mu)(1 + q^2/0.71)^2 = G_{EP}^S/G_{EP}^D$ from the present experiment as a function of q^2. The estimated normalization error of ±4% is not included. The measured form factor seems to fall faster than $1/q^4$ at high q^2.

19. Comparison between several theoretical models and the data in Fig. 18.

20. Comparison between several theoretical models and the data in Fig. 18.

21. Comparison between several theoretical models and the data in Fig. 18.

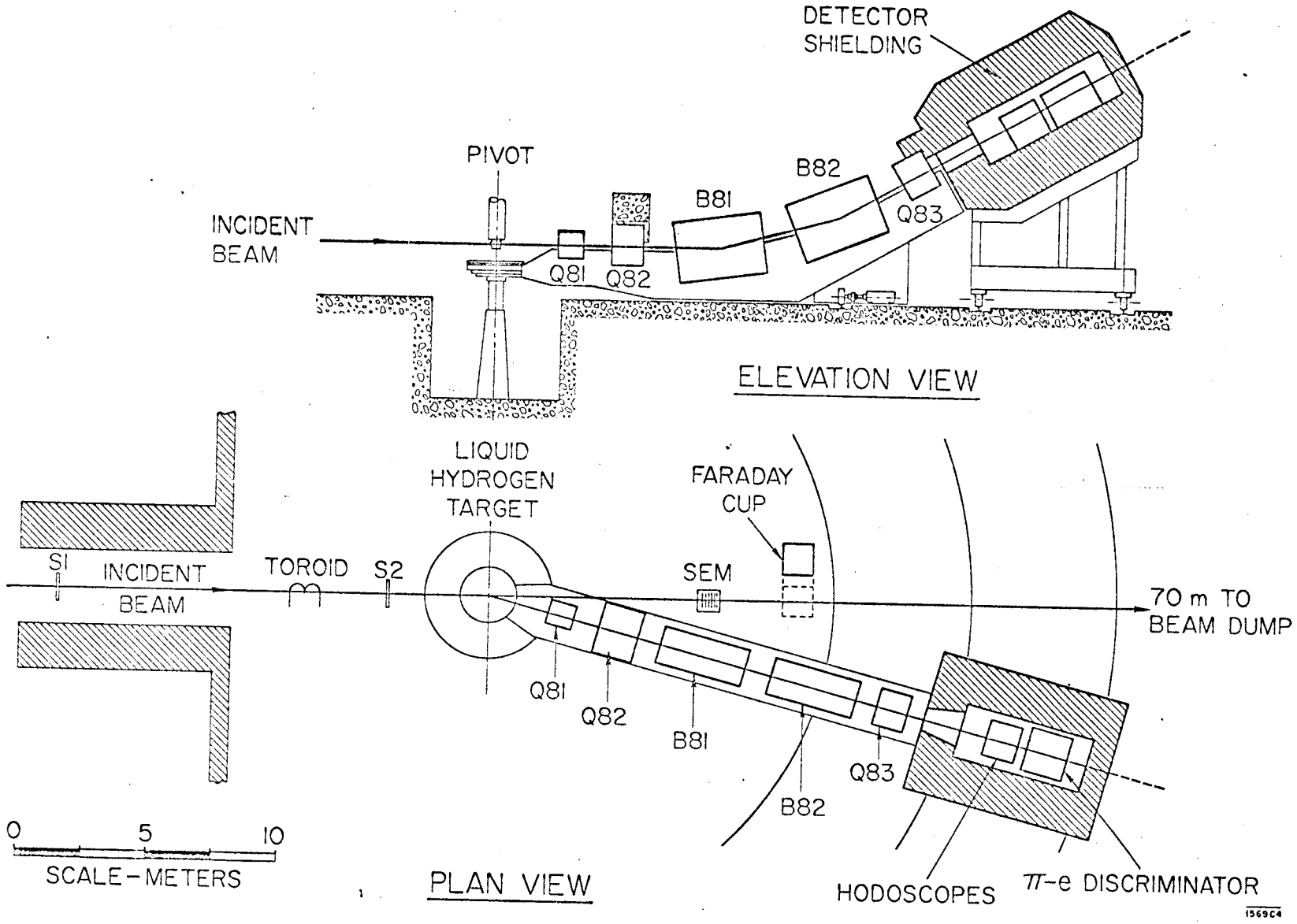
DETECTOR
SHIELDING
PIVOT
B82
B81
Q83
INCIDENT
BEAM
Q81
Q82
ELEVATION VIEW
LIQUID
HYDROGEN
TARGET
FARADAY
CUP
SI
INCIDENT
BEAM
TOROID
S2
SEM
70 m TO
BEAM DUMP
Q81
Q82
B81
Q83
B82
0
5
10
SCALE-METERS
PLAN VIEW
HODOSCOPES
π-e DISCRIMINATOR
156904

FIG. 1

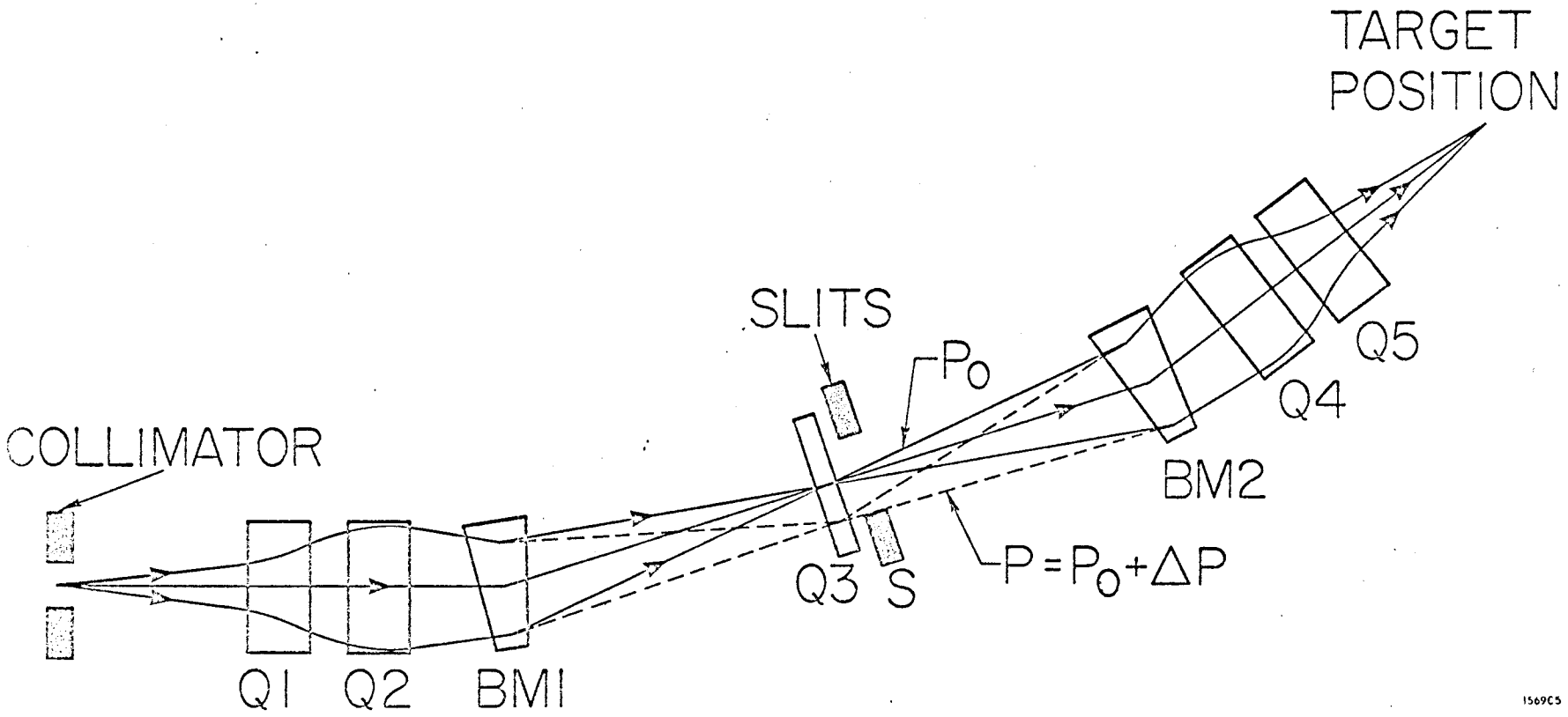
TARGET
POSITION
SLITS
P_0
Q5
Q4
COLLIMATOR
BM2
$P = P_0 + \Delta P$
Q3
S
Q1
Q2
BM1
1569C5

FIG. 2

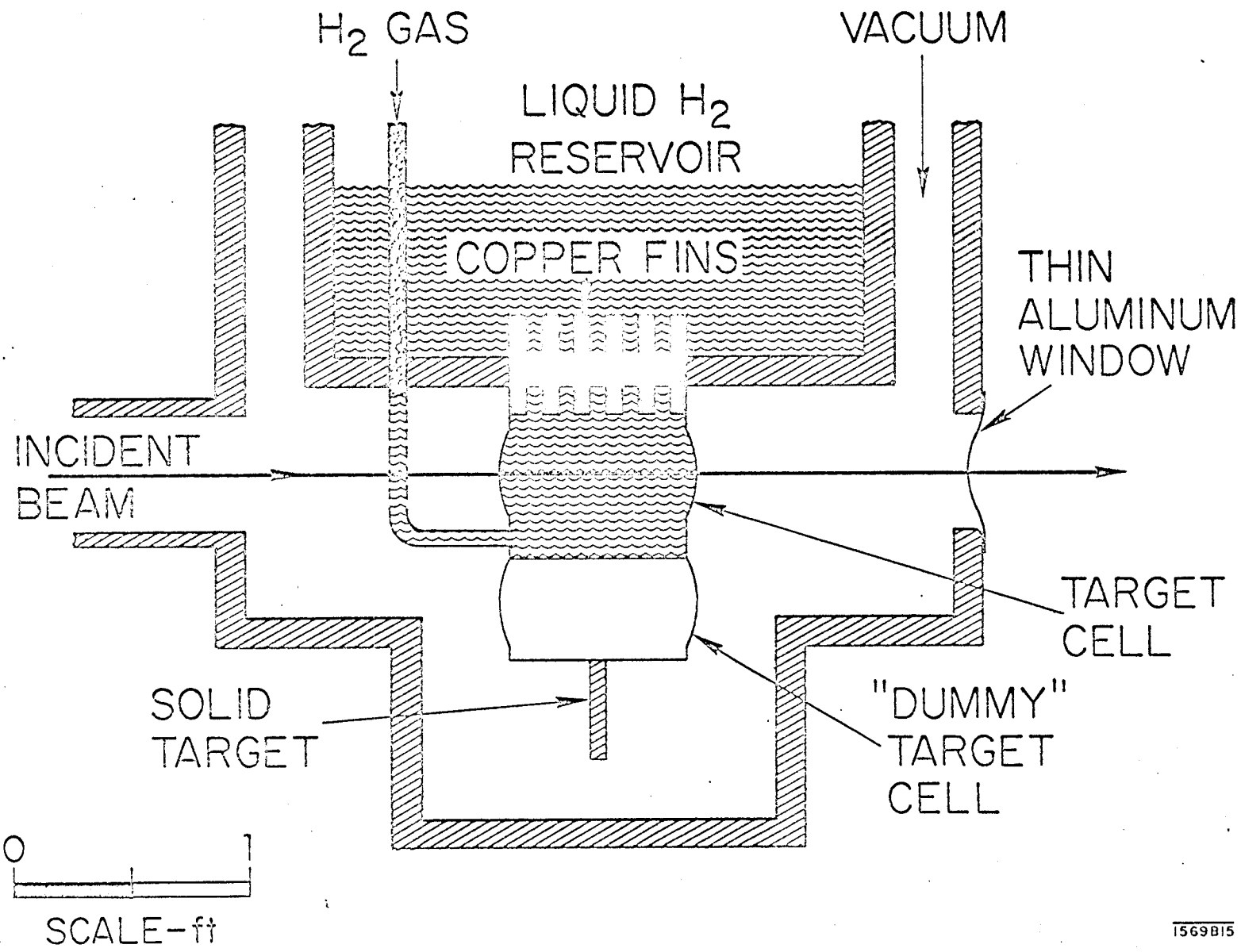
H_2 GAS
VACUUM
LIQUID H_2
RESERVOIR
COPPER FINS
THIN
ALUMINUM
WINDOW
INCIDENT
BEAM
TARGET
CELL
SOLID
TARGET
"DUMMY"
TARGET
CELL
0
1
SCALE-ft
1569B15

FIG. 3

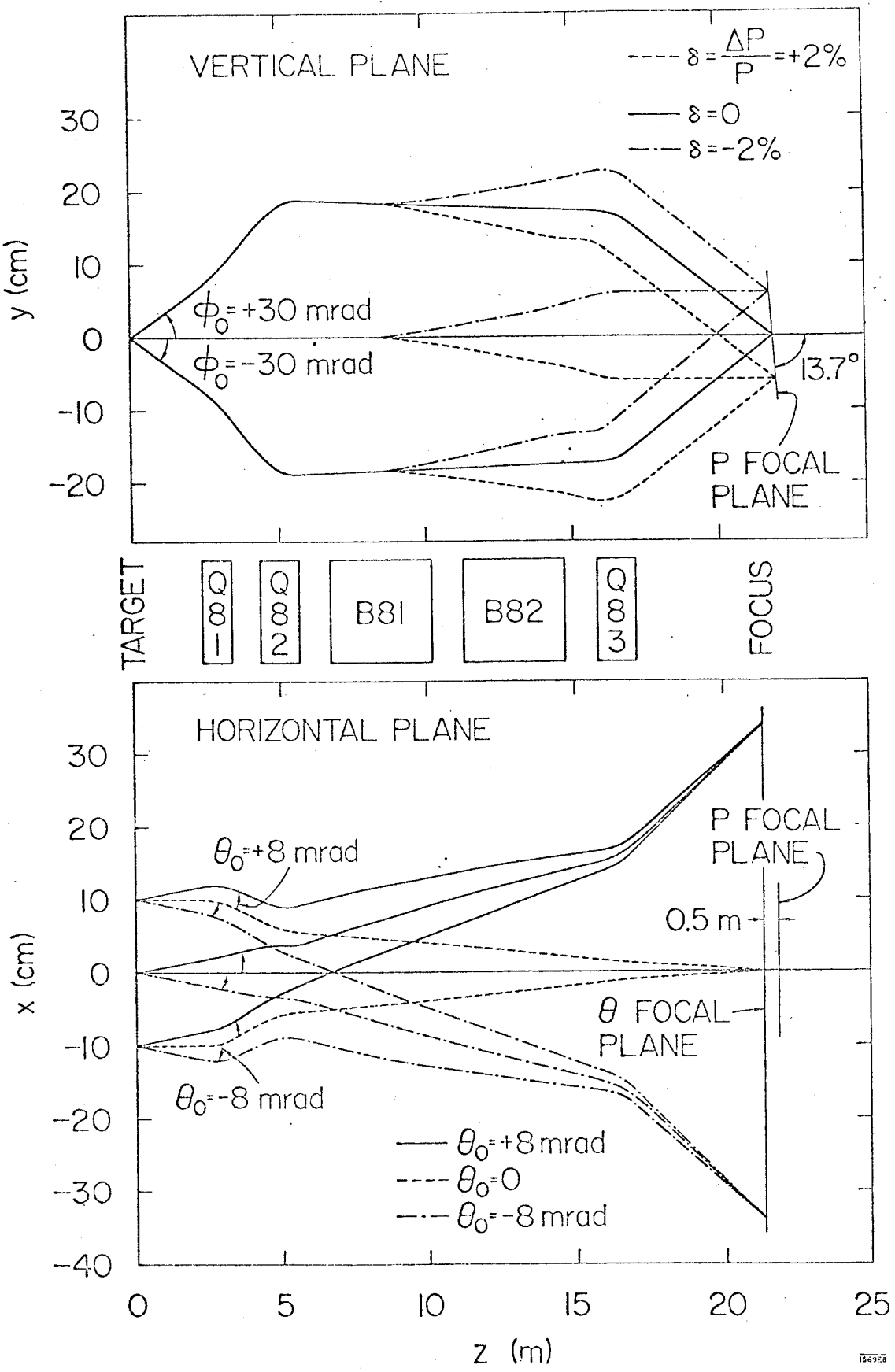
VERTICAL PLANE
δ = ΔP/P = +2%
δ = 0
δ = -2%
y (cm)
30
20
10
0
-10
-20
φ0 = +30 mrad
φ0 = -30 mrad
13.7°
P FOCAL PLANE
TARGET
Q 8 1
Q 8 2
B81
B82
Q 8 3
FOCUS
HORIZONTAL PLANE
x (cm)
30
20
10
0
-10
-20
-30
-40
θ0 = +8 mrad
θ0 = -8 mrad
P FOCAL PLANE
0.5 m
θ FOCAL PLANE
θ0 = +8 mrad
θ0 = 0
θ0 = -8 mrad
0
5
10
15
20
25
z (m)

FIG. 4

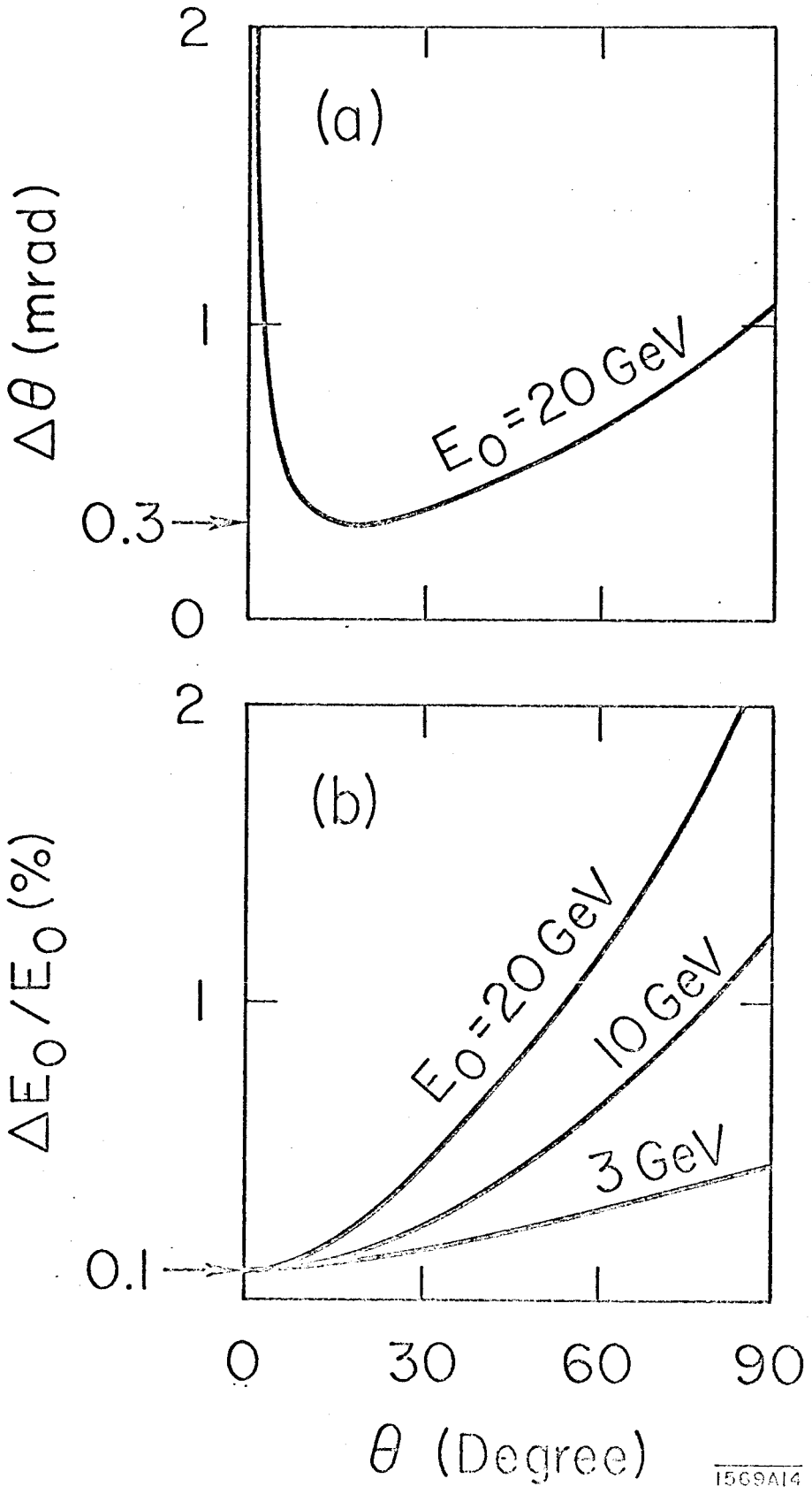
2
(a)
Δθ (mrad)
1
E0=20 GeV
0.3
0
2
(b)
ΔE0/E0 (%)
1
E0=20 GeV
10 GeV
3 GeV
0.1
0
30
60
90
θ (Degree)
1569A14

FIG. 5

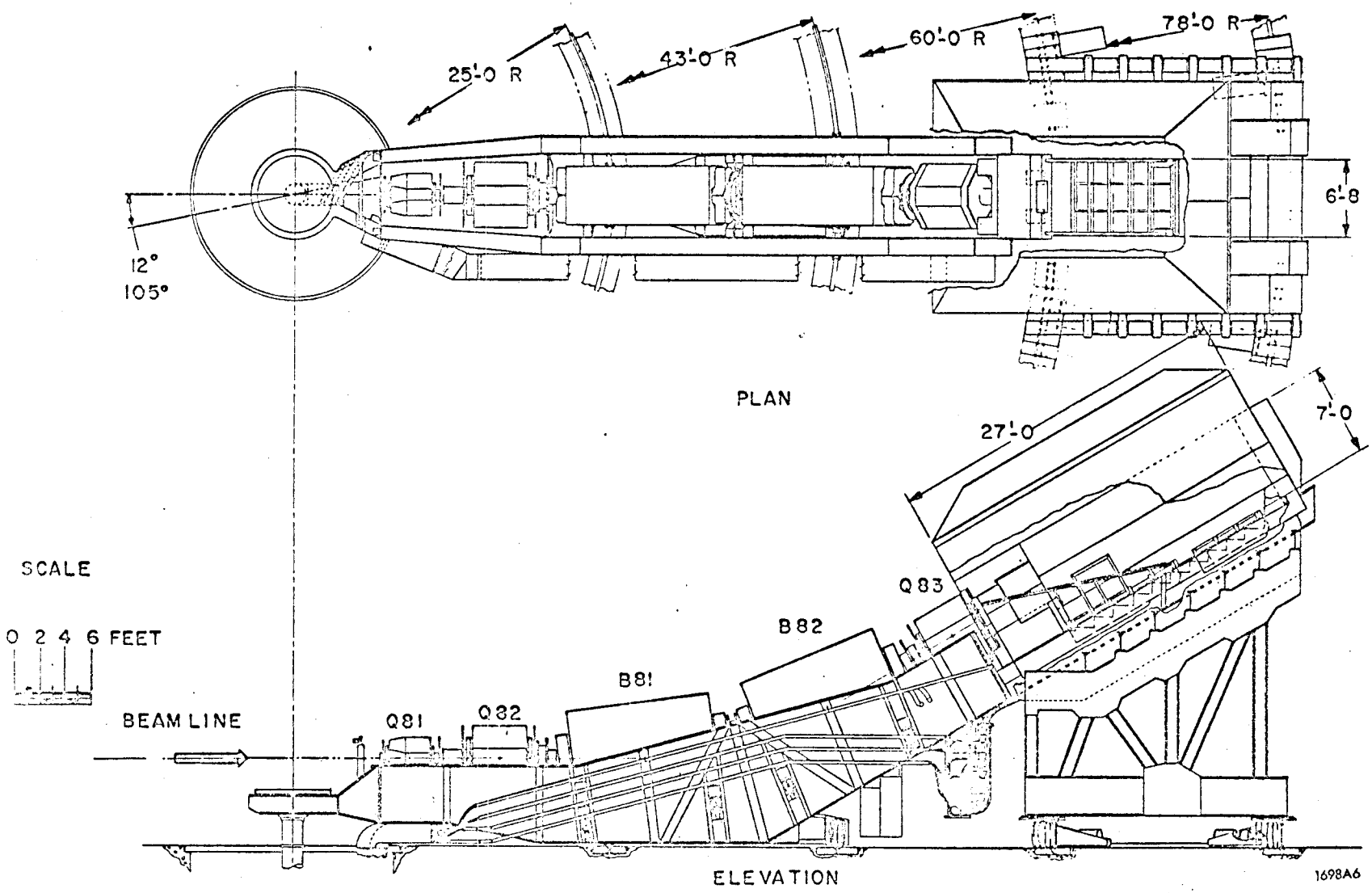
25'-0 R
43'-0 R
60'-0 R
78'-0 R
6'-8
12°
105°
PLAN
27'-0
7'-0
SCALE
0 2 4 6 FEET
BEAM LINE
Q81
Q82
B81
B82
Q83
ELEVATION
1698A6

FIG. 6

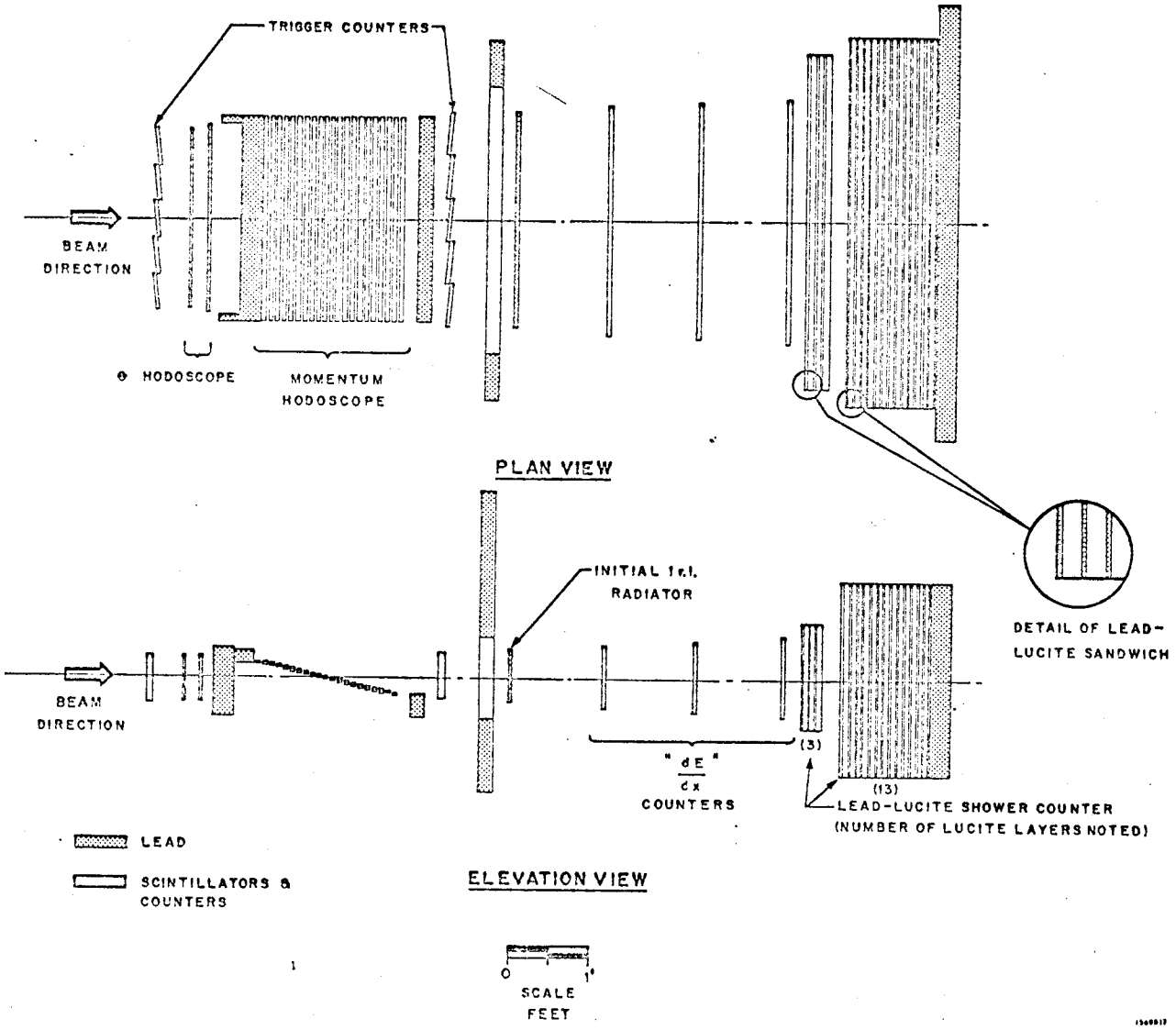
TRIGGER COUNTERS
BEAM DIRECTION
Θ HODOSCOPE
MOMENTUM HODOSCOPE
PLAN VIEW
INITIAL 1 r.l. RADIATOR
DETAIL OF LEAD-LUCITE SANDWICH
BEAM DIRECTION
"dE/dx" COUNTERS
(3)
(13)
LEAD-LUCITE SHOWER COUNTER (NUMBER OF LUCITE LAYERS NOTED)
LEAD
SCINTILLATORS & COUNTERS
ELEVATION VIEW
0
1'
SCALE FEET

FIG. 7

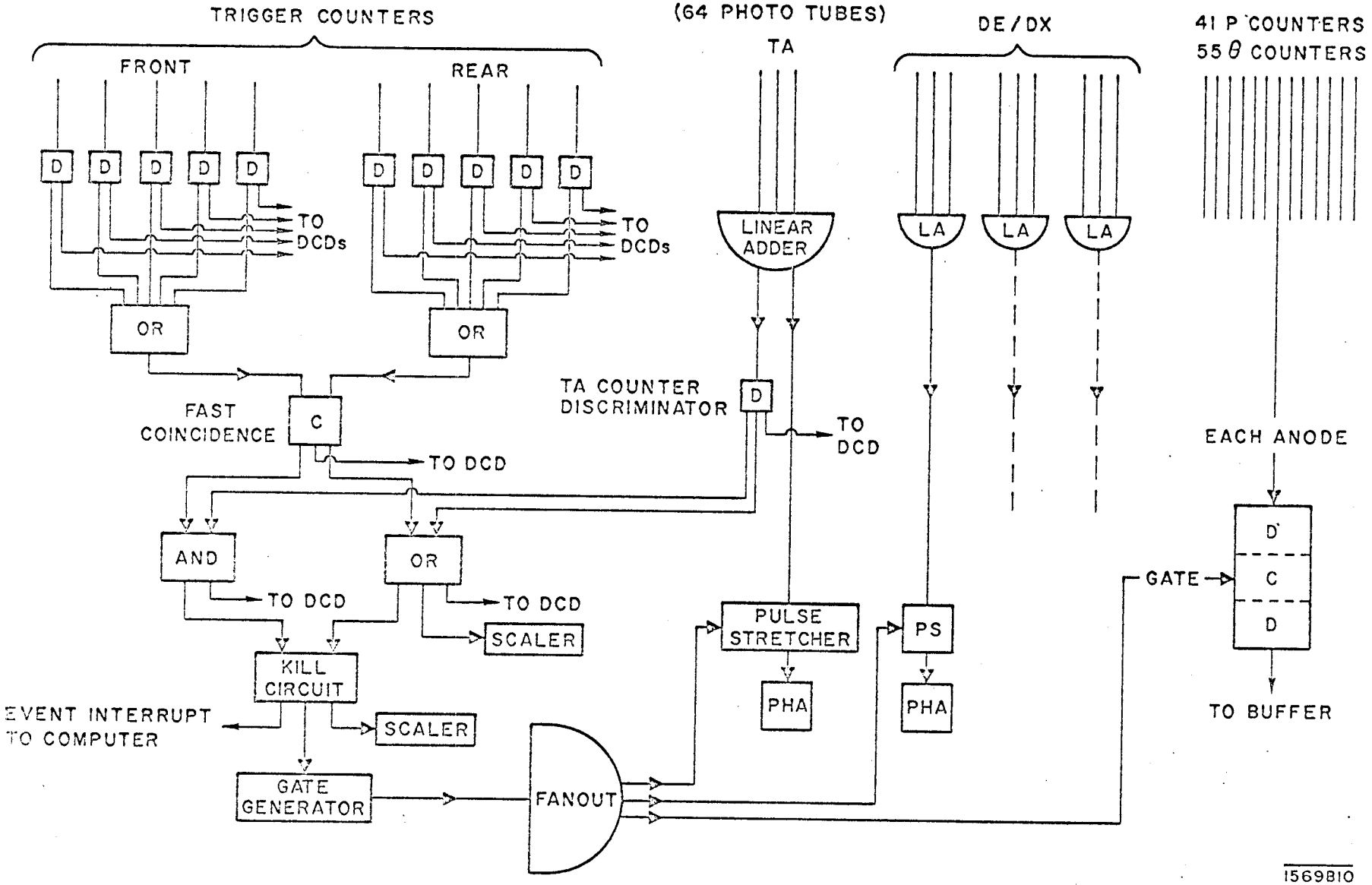
TRIGGER COUNTERS
FRONT
REAR
D
TO DCDs
OR
FAST COINCIDENCE
C
TO DCD
AND
OR
TO DCD
SCALER
KILL CIRCUIT
EVENT INTERRUPT TO COMPUTER
SCALER
GATE GENERATOR
(64 PHOTO TUBES)
TA
LINEAR ADDER
TA COUNTER DISCRIMINATOR
D
TO DCD
PULSE STRETCHER
PHA
DE/DX
LA
PS
PHA
41 P COUNTERS
55 θ COUNTERS
EACH ANODE
D
C
D
GATE
TO BUFFER
FANOUT
1569810

FIG. 8

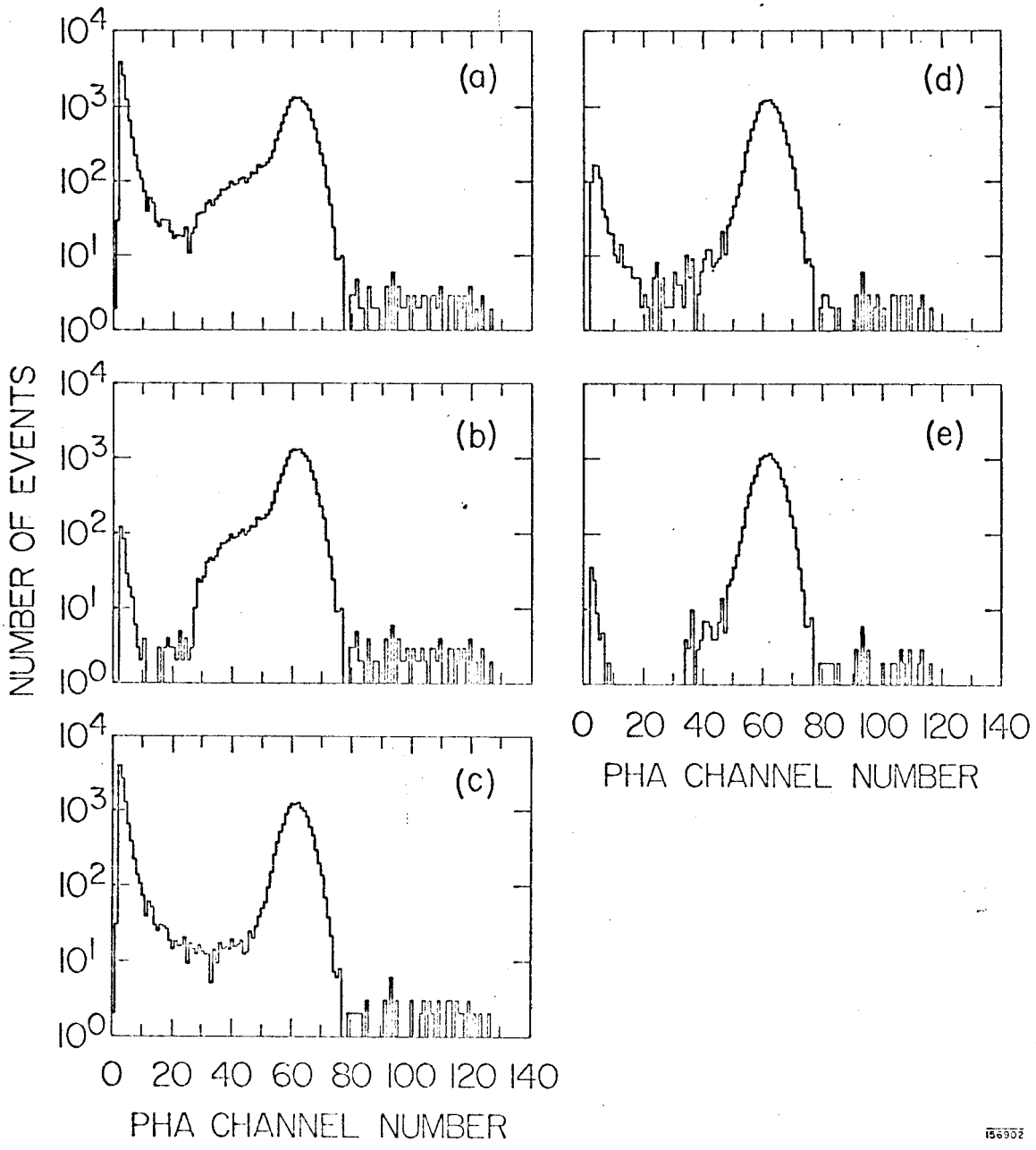
(a)
(b)
(c)
(d)
(e)
NUMBER OF EVENTS
10^4
10^3
10^2
10^1
10^0
0 20 40 60 80 100 120 140
PHA CHANNEL NUMBER
156902

FIG. 9

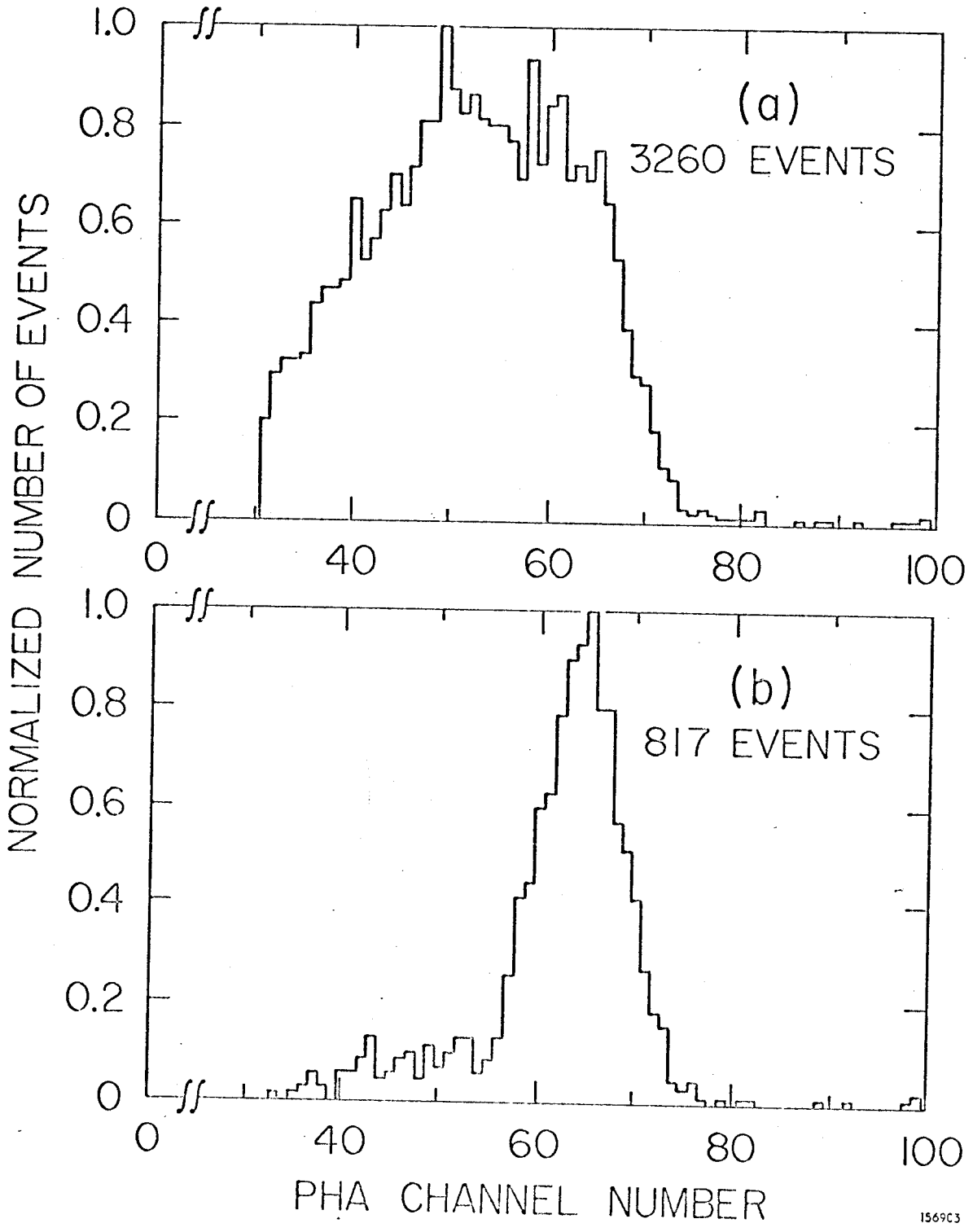
1.0
0.8
0.6
0.4
0.2
0
NORMALIZED NUMBER OF EVENTS
(a)
3260 EVENTS
0
40
60
80
100
(b)
817 EVENTS
PHA CHANNEL NUMBER
156903

FIG. 10

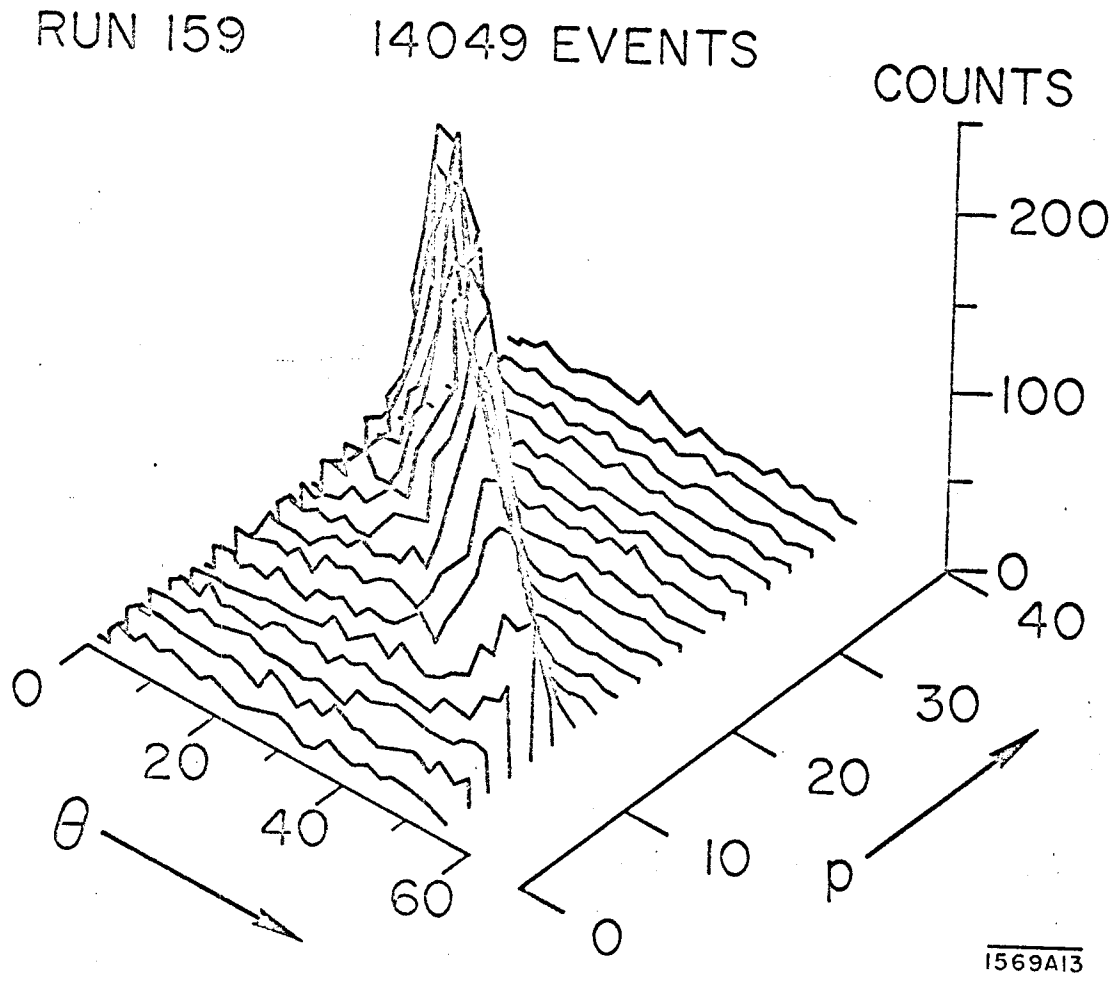
RUN 159
14049 EVENTS
COUNTS
200
100
0
40
30
20
10
0
p
0
20
40
60
θ
1569A13

FIG. 11

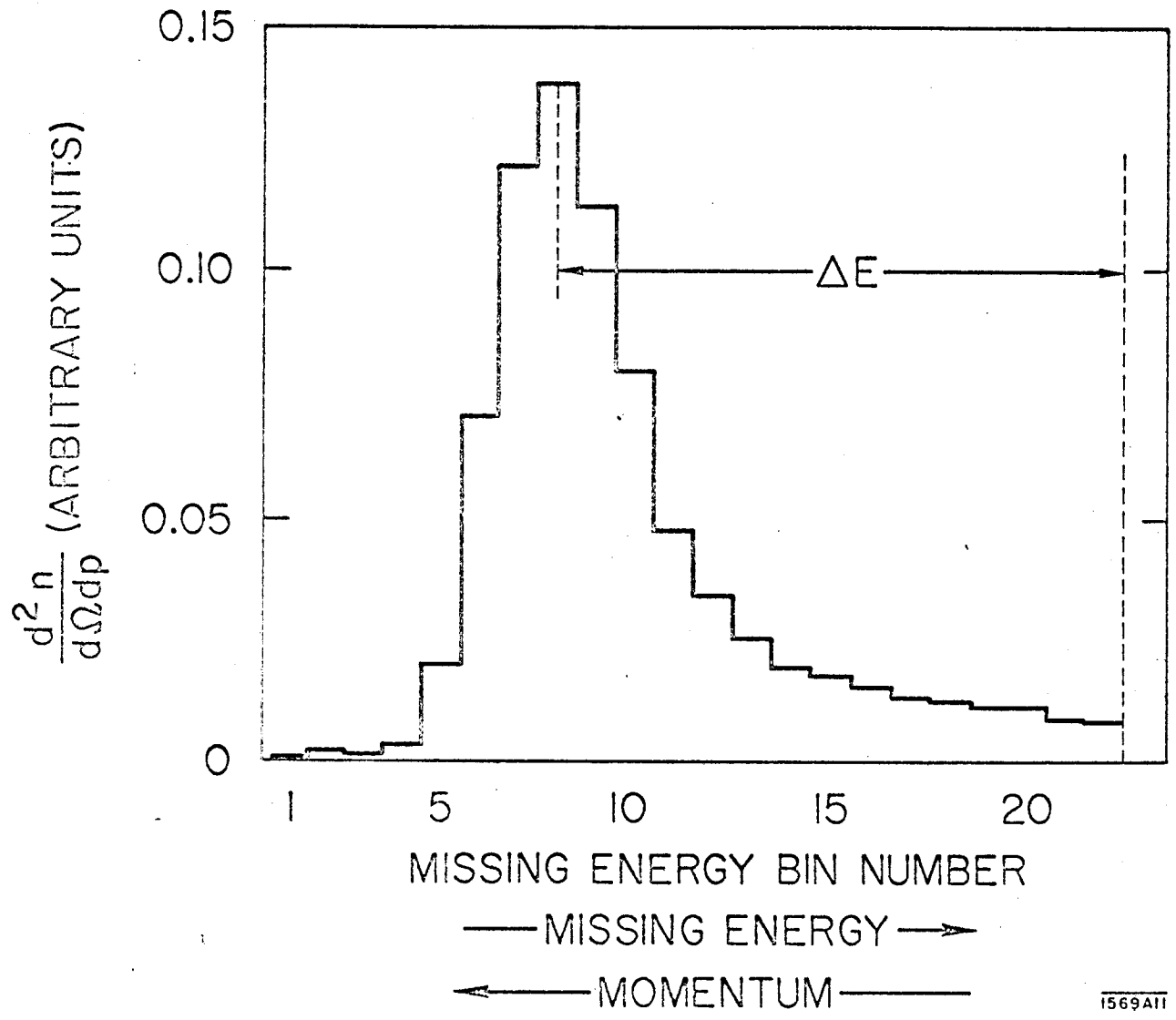
0.15
0.10
0.05
0
$\frac{d^2n}{d\Omega dp}$ (ARBITRARY UNITS)
ΔE
1
5
10
15
20
MISSING ENERGY BIN NUMBER
MISSING ENERGY
MOMENTUM
1569A11

FIG. 12

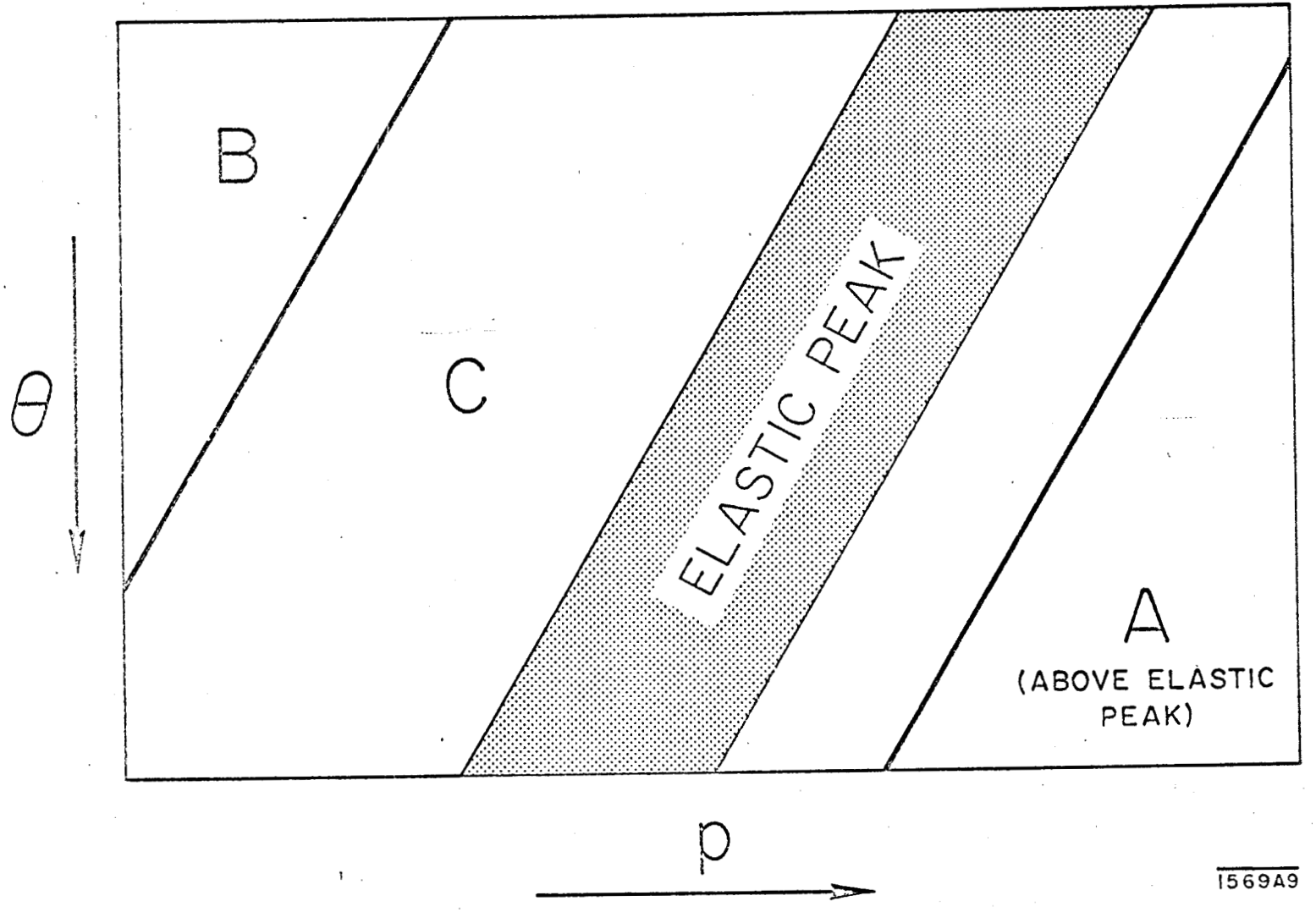

FIG. 13

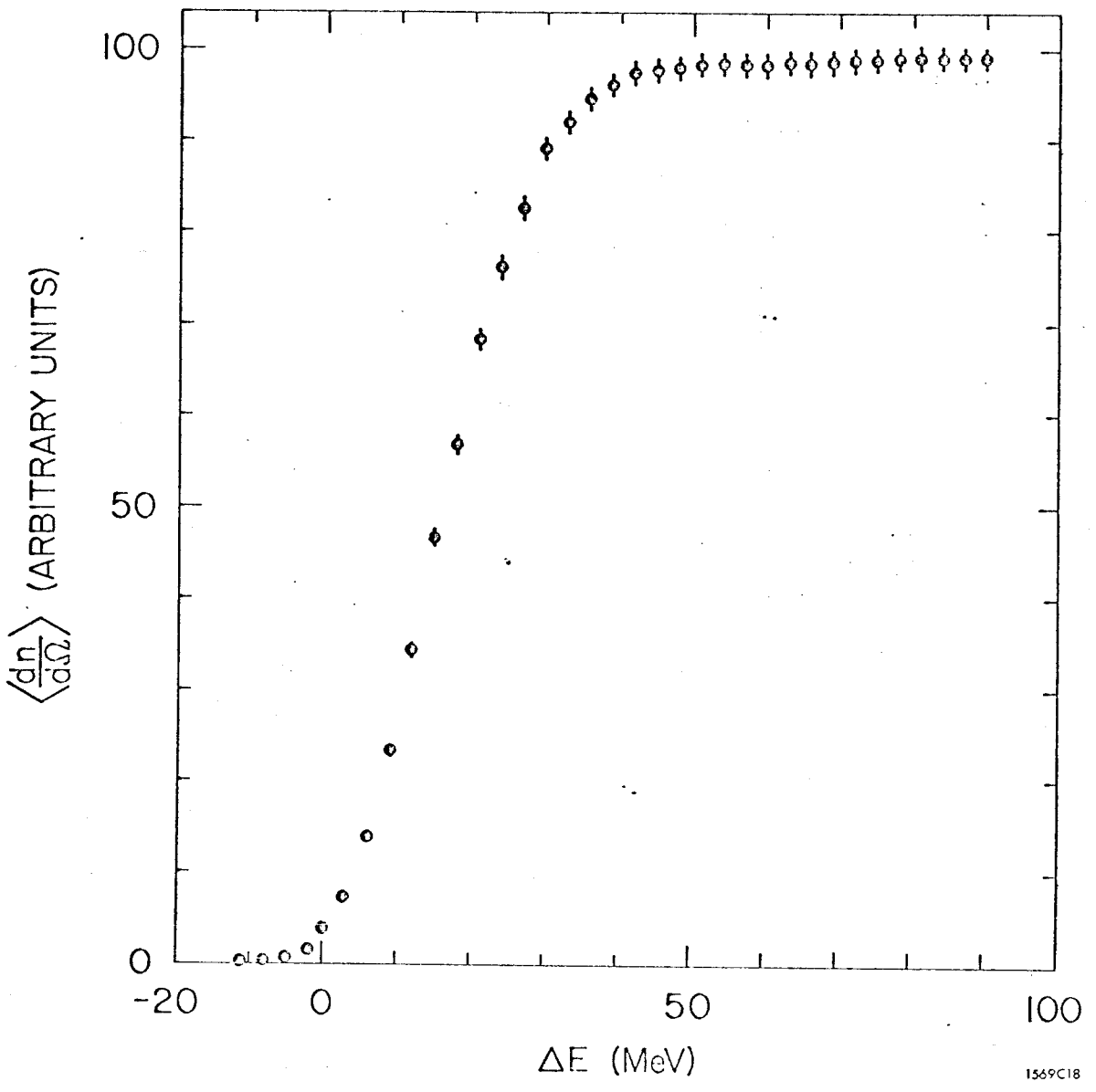
100
50
0
-20
0
50
100
$\left\langle \frac{dn}{d\Omega} \right\rangle$ (ARBITRARY UNITS)
ΔE (MeV)
1569C18

FIG. 14

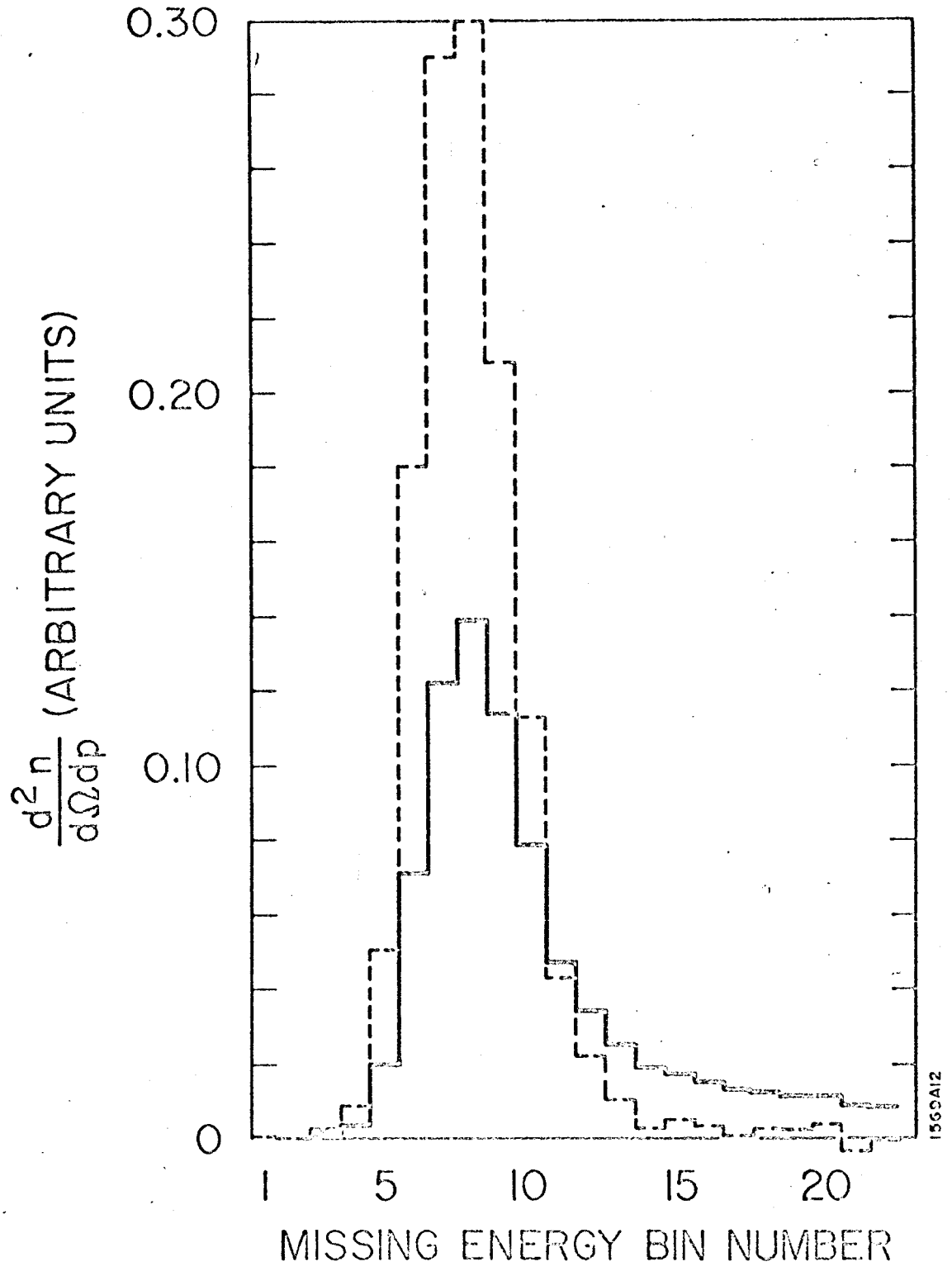
0.30
0.20
0.10
0
$\frac{d^2n}{d\Omega dp}$ (ARBITRARY UNITS)
1
5
10
15
20
MISSING ENERGY BIN NUMBER
1569A12

FIG. 15

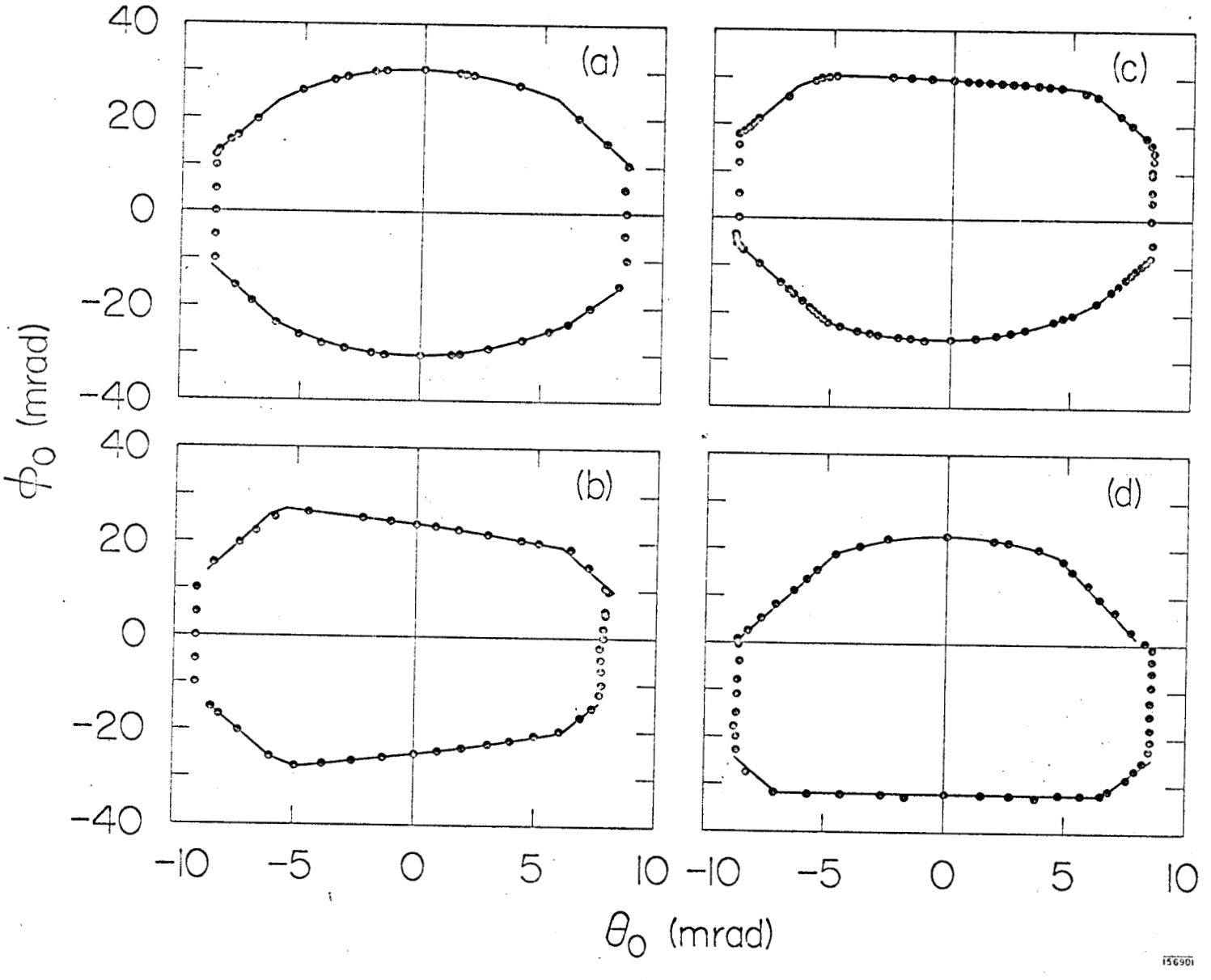

FIG. 16

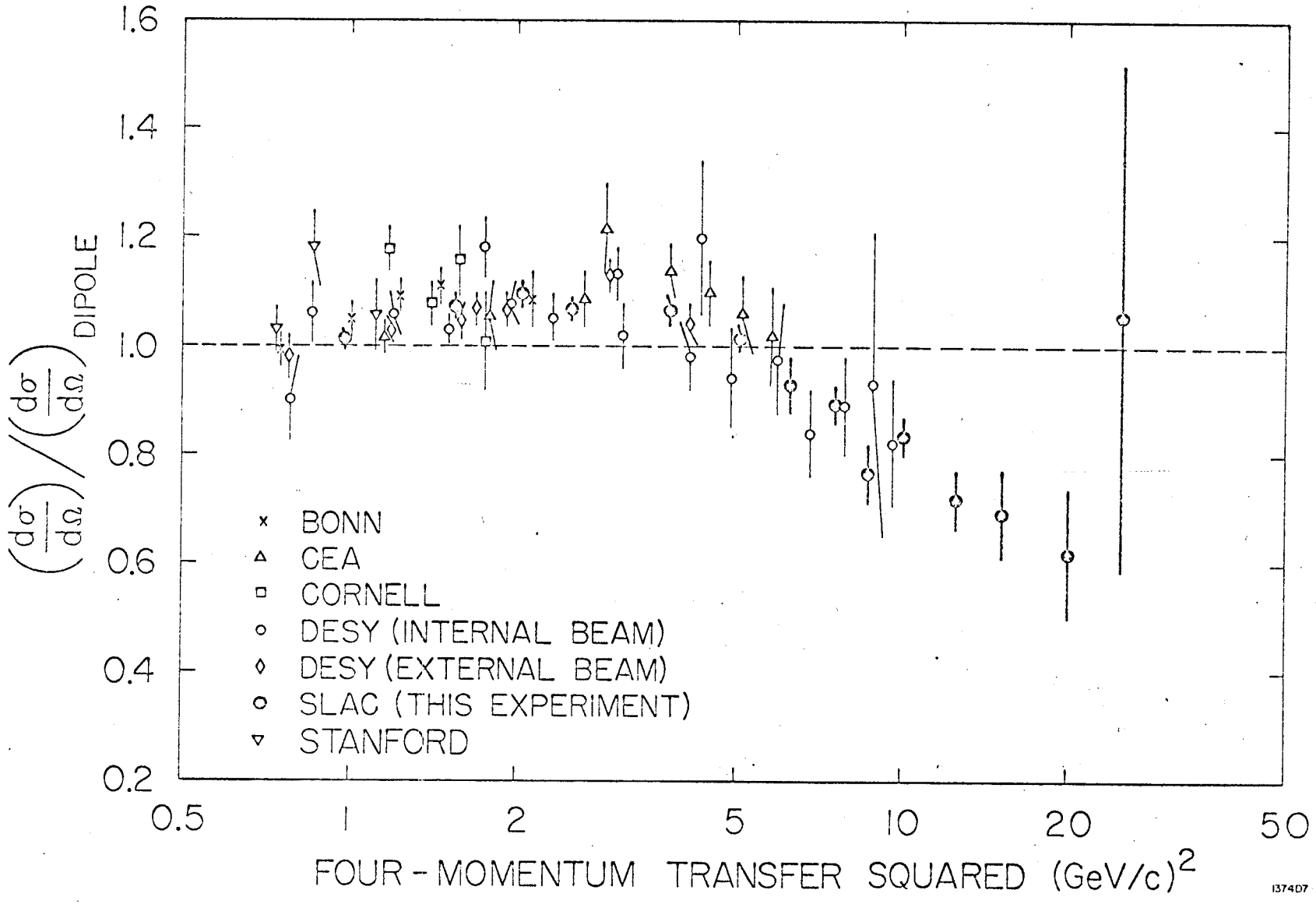
1.6
1.4
1.2
1.0
0.8
0.6
0.4
0.2
$\left(\frac{d\sigma}{d\Omega}\right) / \left(\frac{d\sigma}{d\Omega}\right)_{DIPOLE}$
BONN
CEA
CORNELL
DESY (INTERNAL BEAM)
DESY (EXTERNAL BEAM)
SLAC (THIS EXPERIMENT)
STANFORD
0.5
1
2
5
10
20
50
FOUR-MOMENTUM TRANSFER SQUARED $(GeV/c)^2$
137407

FIG. 17

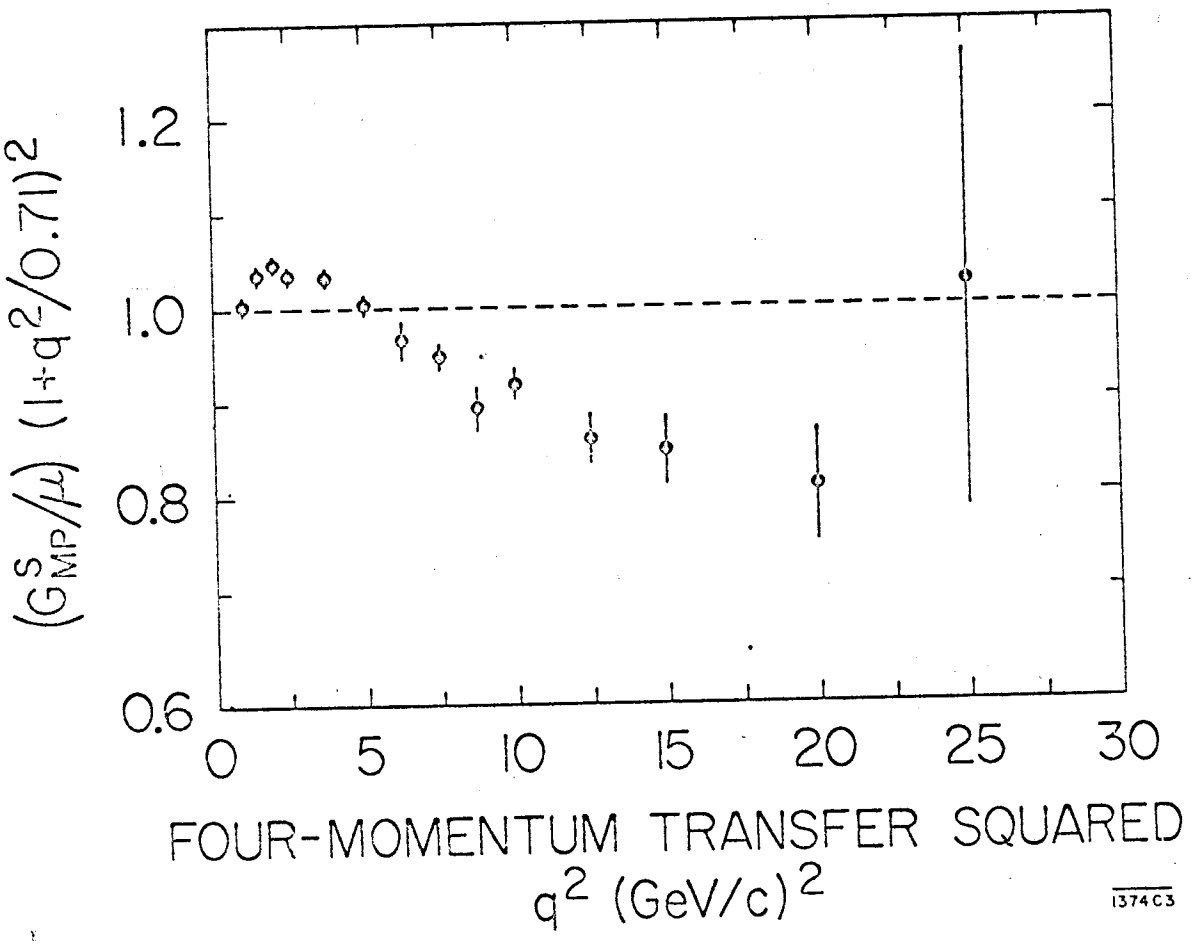
$(G^S_{MP}/\mu)\ (1+q^2/0.71)^2$
1.2
1.0
0.8
0.6
0
5
10
15
20
25
30
FOUR-MOMENTUM TRANSFER SQUARED
q^2 (GeV/c)^2
1374C3

FIG. 18

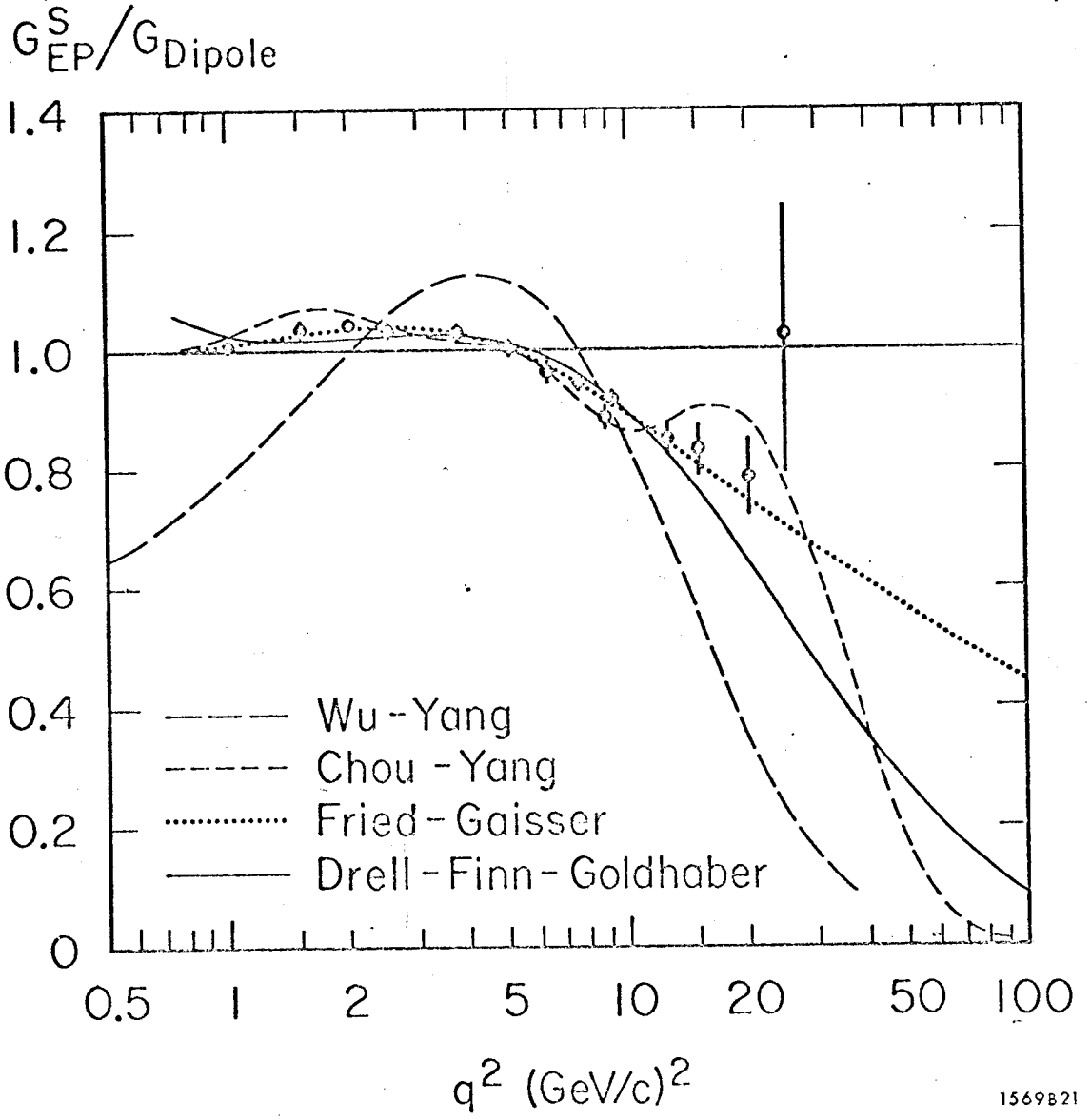
G^S_{EP}/G_{Dipole}
1.4
1.2
1.0
0.8
0.6
0.4
0.2
0
Wu - Yang
Chou - Yang
Fried - Gaisser
Drell - Finn - Goldhaber
0.5
1
2
5
10
20
50
100
q^2 (GeV/c)^2
1569B21

FIG. 19

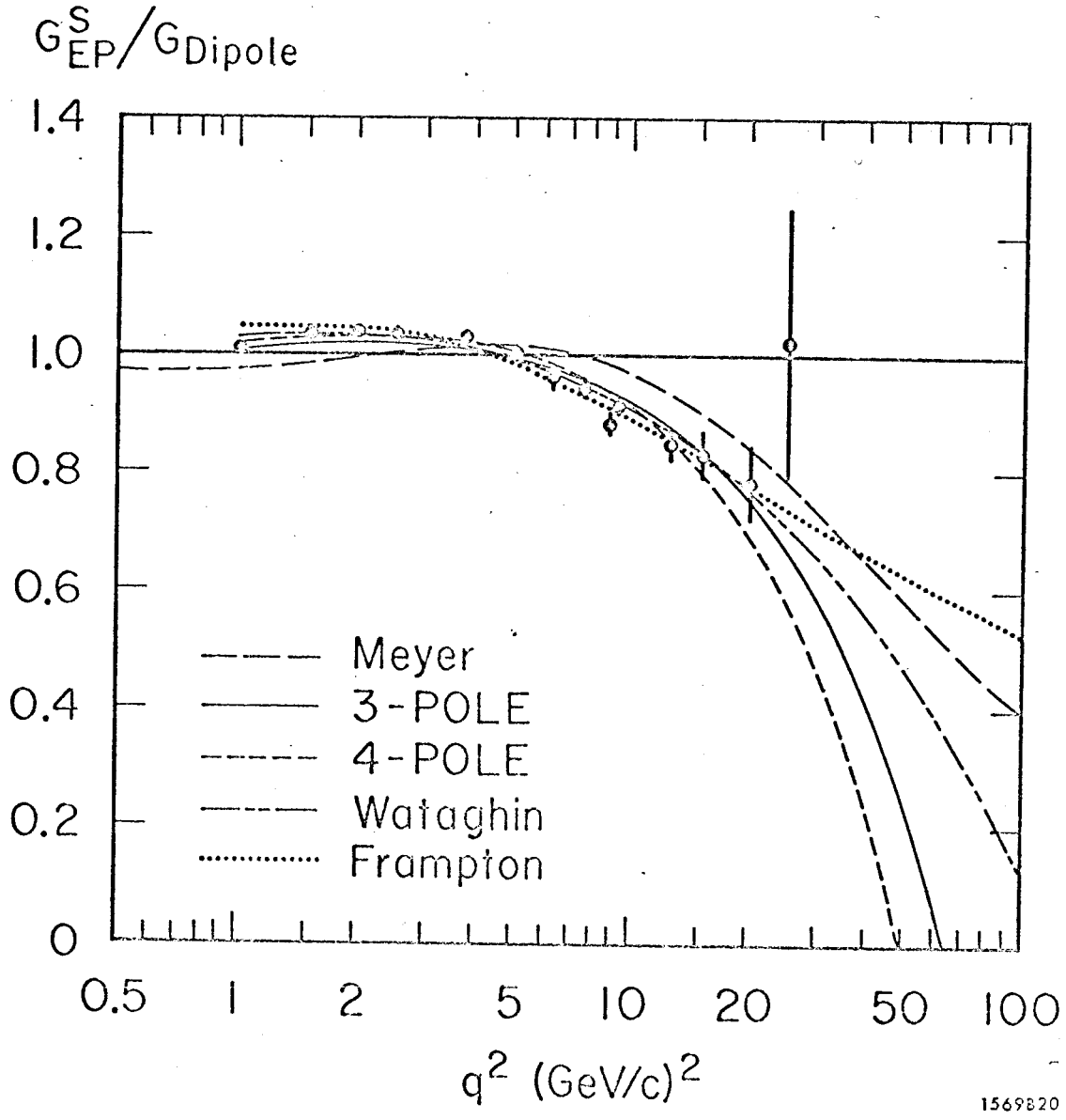
G^S_{EP}/G_{Dipole}
1.4
1.2
1.0
0.8
0.6
0.4
0.2
0
Meyer
3-POLE
4-POLE
Wataghin
Frampton
0.5
1
2
5
10
20
50
100
q^2 (GeV/c)^2
1569820

FIG. 20

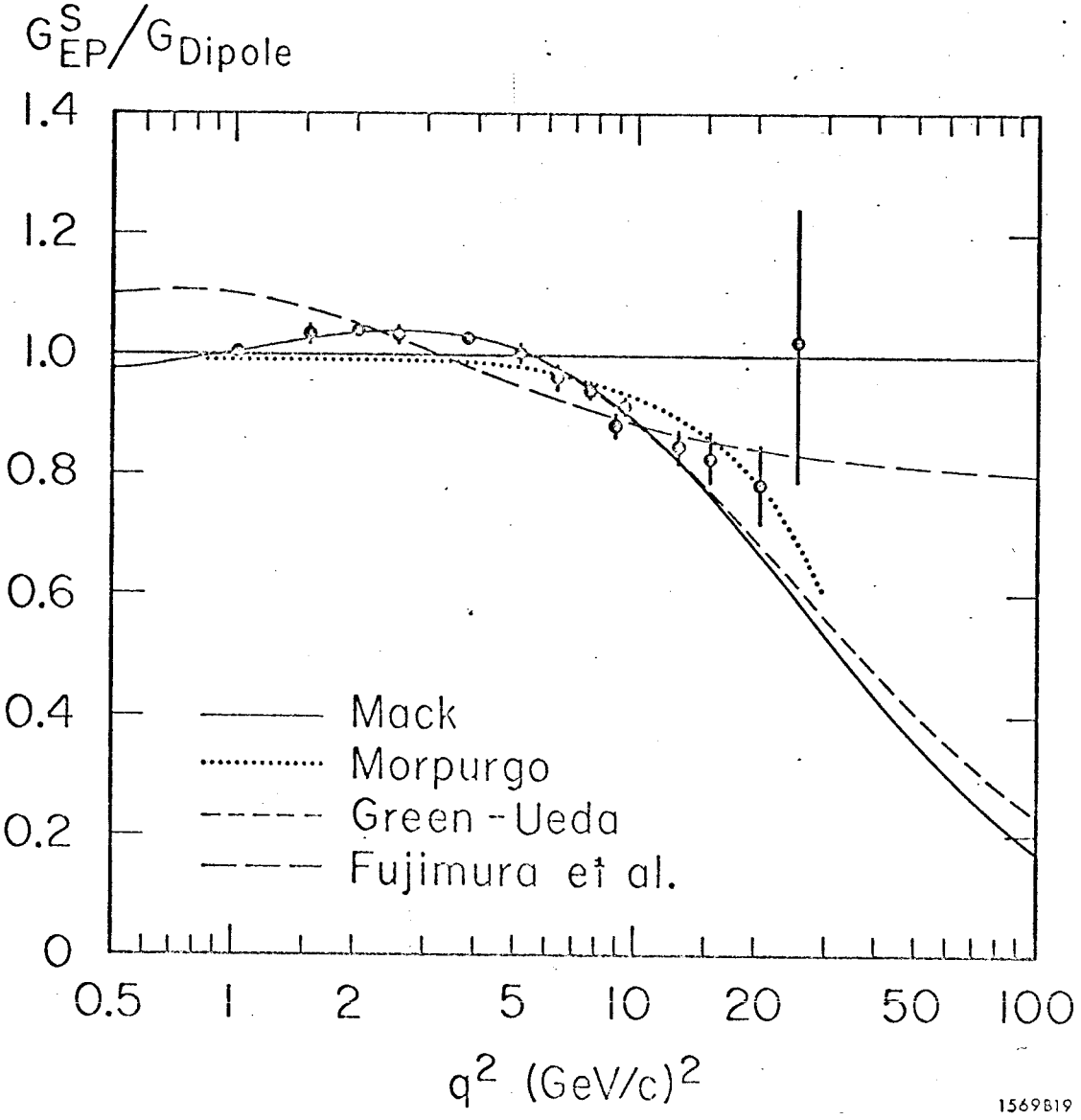
G^S_{EP}/G_{Dipole}
1.4
1.2
1.0
0.8
0.6
0.4
0.2
0
0.5
1
2
5
10
20
50
100
q^2 (GeV/c)^2
Mack
Morpurgo
Green - Ueda
Fujimura et al.
1569B19

FIG. 21